Energetic electron enhancements under radiation belt (L < 1.2) during nonstorm interval on August 1, 2008

Alla V. Suvorova [1,3], Alexei V. Dmitriev[2,3], and Vladimir A. Parkhomov[4]

[1] GPS Science and Application Research Center, National Central University, Jhongli, Taiwan
[2] Institute of Space Science, National Central University, Jhongli, Taiwan
[3] Skobeltsyn Institute of Nuclear Physics, Lomonosov Moscow State University, Moscow, Russia
[4] Baikal State University, Irkutsk, Russia

Correspondence to: Alla Suvorova (suvorova_alla@yahoo.com)

Abstract

An unusual event of deep injections of >30 keV electrons from the radiation belt to low *L* shells (*L* < 1.2) in midnight-dawn sector was found from NOAA/POES observations during quiet geomagnetic conditions on August 1, 2008. Using THEMIS observations in front of the bow shock, we found transient foreshock conditions and IMF discontinuities passing the subsolar region at that time. These conditions resulted in generation of plasma pressure pulses and fast plasma jets observed by THEMIS, respectively, in the foreshock and magnetosheath. Signatures of interactions of pressure pulses and jets with the magnetopause were found in THEMIS and GOES measurements in the dayside magnetosphere and ground magnetogram records from INTERMAGNET. The jets produce penetration of hot magnetosheath plasma into the dayside magnetosphere as were observed by the THEMIS probes after approaching the magnetopause. High-latitude precipitation of the hot plasma were observed by NOAA/POES satellites on the dayside. The precipitations preceded the >30 keV electron injections at low latitudes. We propose a scenario of possible association between the phenomena observed.

Key words: quasi-trapped energetic electrons, deep particle injections, plasma jets, subsolar foreshock

1. Introduction

Deep injections of tens to hundreds of keV particles into the inner radiation belt, i.e. drift shells L < 3, during quiet or weak geomagnetic activity have recently become one of the main issues of radiation belt dynamics (e.g., Park et al., 2010; Zhao and Li, 2013; Turner et al., 2017). Injection or transport of particles implies violation of adiabatic motion and changing of L-shell. The cause of nonstorm injections has not yet been understood.

The mechanisms responsible for the violation of adiabatic motion of energetic particles at low L were a subject of resent studies. The studies presented some intriguing challenges for current models of energetic particle injections. Observations showed that tens to hundreds of keV electrons penetrate deeper than MeV energy electrons (e.g., Zhao and Li, 2013). The keV-energy electrons can often penetrate down to the slot region separating the inner and outer radiation belts (L ~ 2.5 - 3.5) and into the inner radiation belt at L < 2 (e.g., Turner et al., 2017). Moreover, the deepest penetrations of energetic electrons were revealed even below the inner radiation belt at L < 1.2 (Asikainen and Mursula, 2005; Suvorova et al. 2012; 2013; Dmitriev et al., 2017).

From a comparison of deep penetrations of electrons and protons, Zhao et al., (2017a) have revealed principle differences in these phenomena suggesting different underlying physical mechanisms responsible for deep penetrations of protons and electrons. Particularly, deep proton penetration is consistent with convection of plasma sheet protons, and deep electron penetration suggests the existence of a local time localized mechanism. Moreover, Turner et al. (2015; 2017) showed that the deep injections of electrons at L<4 resulted from a different mechanism than injections observed at higher L shells. Particularly, Turner et al. (2015) hypothesized that the mechanism could be related to wave activity in the Pi2 frequency range, which usually serves as an indicator of substorm activity. Overall, dynamics of the tens to hundred keV electrons at low L-shells is very different from dynamics of both protons and electrons at higher L-shells and also in higher energy range. The electron injections at L <3 cannot be explained by an enhanced convection electric field, convection of plasma sheet electrons or inward radial diffusion (e.g., Turner et al., 2017; Zhao et al., 2017a)

The ability of energetic electrons to penetrate deeply in the inner zone and below is still puzzling. An answer to the question may be found by investigating the relation of deep injections of energetic electrons to solar wind parameters, geomagnetic activity indices and other parameters of magnetospheric and ionospheric responses (Suvorova, 2017; Zhao et al., 2017b). Rapid enhancements of electron fluxes in the inner zone and below have been known for a long time in association with strong magnetic storms (e.g., Krasovskii et al., 1961; Savenko et al., 1962; Pfitzer and Winckler, 1968). However, increased statistics have revealed that deep injections of keV-energy electrons may occur frequently, and furthermore, regardless of storm strength (Tadokoro et al., 2007; Park et al., 2010; Zhao and Li, 2013; Suvorova et al., 2013, 2016).

The statistical study by Suvorova (2017) showed that electron injections into the forbidden zone ($L < 1.2$) are relatively rare and occur mostly during magnetic storms and substorms. But sometimes, they also occur during nonstorm conditions and weak substorm activity. This fact is consistent with the recent finding of “quiet” injections in the inner radiation belt mentioned above. A case of “quiet” injections of energetic electrons at $L < 1.2$ is in the focus of our study.

Here, we summarize the main characteristics of the electron injections into the very low L-shells from several papers (Suvorova and Dmitriev, 2015; Suvorova, 2017; Dmitriev et al., 2017). The quasi-trapped energetic electron population in the forbidden zone, referred to as forbidden energetic electrons (FEE), can be characterized as transient with highly variable fluxes. The behavior of FEE is similar to keV energy trapped electrons in the inner radiation belt with flux enhancements in response to magnetic storms (e.g., Tadokoro et al., 2007; Dmitriev and Yeh, 2008; Zhao et al., 2017a). Simultaneous measurements of particles by satellites at different altitudes provided clear evidence that the forbidden zone enhancements of energetic electrons were caused by fast penetration of the inner belt electrons (Suvorova et al., 2014). As known, an important role in fast transport of particles during storms is played by magnetic and electric field perturbations. Such perturbations are usually associated with the influence of magnetospheric substorms, or nighttime processes of magnetic field dipolarizations in the magnetotail (e.g., Glocer et al., 2011). However, substorm signatures in the magnetic field in the low-L region (L< 2) have never been observed.

The most probable mechanism of the FEE injections was suggested as the *ExB* drift (Suvorova et al., 2012), and most of researchers consider and model an electric drift of inner belt electrons in the *ExB* fields, even though the electric field must be very high (e.g., Zhao and Li, 2013; Lejosne and Mozer, 2016; Selesnick et al., 2016; Su et al., 2016). According to simulation results of Selesnick et al. (2016), the electric field of ~5 mV/m can provide deep injections at L<1.3. There is no explanation for penetration of a strong electric field to such low *L*-shells. What is more important, there is no reliable information on electric fields at heights of 500-2000 km, because measurements there are difficult, and, as a consequence of this, empirical electric field models are limited and do not provide the results below L~2 (e.g., Rowland and Wygant, 1998; Matsui et al., 2013). The most modern research suggests that the actual strength of penetration electric fields can be stronger than any existing electric field model at L < 2 (Su et al., 2016).

A relation between the FEE injections and geomagnetic activity was studied in (Suvorova et al., 2013; 2014). It seemed for a while that intense geomagnetic activity like auroral substorms was one of the necessary factors for deep electron injections, and the storm-time *Dst*-variation did not control the FEE occurrences (Suvorova et al., 2014). It was suggested that substorm-associated strong electric field can penetrate to the low *L* region, thereby creating the conditions for fast earthward transport of trapped electrons in crossed E and B fields. Note that recent modeling of the *ExB* transport mechanism at *L* < 1.3 demonstrated that the mechanism can successfully operate in the low *L* region (Selesnick et al., 2016).

However, after that, many FEE events were found during moderate and weak auroral activity, which was typical for pre-storm (initial phase) or even non-storm conditions and, moreover, high AE index does not always guarantee injections (Suvorova and Dmitriev, 2015). Indeed, statistically, such a casual relationship with substorms was not confirmed (Suvorova, 2017). From total statistics of ~530 days with FEE enhancements collected during two solar cycles, more than three dozen days without essential substorm activity were found. These “quiet” events occurred over past decade from 2006 to 2016. The FEE enhancements in that case were observed only in low energy range of tens of keV.

It is important to mention that one interesting feature was unexpectedly found from the statistical study. It is that the most favorable conditions for the FEE enhancements arise in the period from May to September independently on geomagnetic activity level. A second, minor peak of the occurrence appears in the December - January period. Suvorova (2017) suggested an important role of the auroral ionosphere in the occurrence of FEE injections. The peculiar annual variation of the FEE occurrence rate was explained by a change in conductance of the auroral ionosphere. The conductance depends directly on the illumination of the noon sector of the auroral zone. A seasonal variation (summer-winter asymmetry) of dayside conductance was demonstrated by Sibeck et al. (1996). As known, the high-latitude ionosphere is better illuminated during solstice periods, with that the illumination of the northern region is higher than the illumination of the southern one because of the dipole axis offset relative to the Earth’s center. This fact can explain an existence of two peaks of the FEE occurrence with the major one during the northern summer period.

External drivers from the solar wind should trigger some processes in the magnetosphere-ionosphere system that might result in the electron injections into the forbidden zone. However, the external drivers are necessary but often not sufficient for FEE enhancements to occur. If the auroral ionosphere is sunlit, then impact of external drivers more likely results in the electron injections into the forbidden zone. In this case, the factor of the dayside auroral ionosphere conductivity is sufficient, and it comes to the fore during weak geomagnetic activity. The relevant processes in the magnetosphere-ionosphere chain during magnetic quiet are still unclear. A comprehensive analysis of the solar wind drivers and magnetospheric response may help us to lift the veil. In this paper, we study prominent FEE enhancements during nonstorm condition on August 1, 2008 in order to determine their possible drivers in the solar wind. Note that this event is a subset (1%) of the total statistics collected by Suvorova (2017) during various conditions, from magnetic quiet to extremely strong geomagnetic storms.

2. Observations on August 1, 2008

2.1. Forbidden Electron Enhancements

Figure 1 shows large enhancements of the >30 keV electron fluxes at low latitudes on August 1, 2008. The data were compiled from all orbital passes of five NOAA/POES satellites. The electron fluxes in the energy ranges >30, >100 and >300 keV were measured by the MEPED instruments boarded on each satellite. The MEPED instrument includes two identical electron solid-state detector telescopes and measures particle fluxes in two directions: along and perpendicular to the local vertical direction (Evans and Greer, 2004). The data shown in Figure 1 are from the 0-degree telescope oriented along the orbital radius-vector (i.e. vertically), so that it measured quasi-trapped particles near the equator and precipitating particles in the auroral region. The forbidden zone is defined as $L < 1.2$ in the longitudinal range from 0° to 260°E (or 100°W) that is beyond the South Atlantic anomaly (SAA). The drift L-shells are calculated from IGRF-2005 model. Figure 1a shows the observations of >30 keV electrons at 0 - 12 UT. At that time, the satellites passed the same regions but they did not detect any FEE enhancements. Figure 1b shows the interval 12 - 24 UT, when fluxes of >30 keV quasi-trapped electrons in the forbidden zone increased by 3 orders of magnitude above a background of ~10^2 (cm^2 s sr)$^{-1}$.

We have selected FEE enhancements with intensity >10^3 (cm^2 s sr)$^{-1}$. As found previously, the flux enhancements at low latitudes are peculiar to the quasi-trapped energetic electrons (Suvorova et al., 2012). In contrast, enhancements of electrons precipitating at low latitudes are very rare, weak and short. During the event, precipitating electron fluxes in the forbidden zone did not increase (not shown). Fluxes of the precipitating and quasi-trapped >100 keV electrons and >30 keV protons did not increase also (not shown). The quasi-trapped electrons are mirroring at heights below the satellite orbit (~850 km) in a region of ±30° latitudes, and drift eastward with a rate of 17°-19° per hour toward the SAA area, where they are lost due to scattering in the dense atmosphere.

Figure 2 and Table 1 present main characteristics of 15 FEE enhancements detected along equatorial passes of NOAA/POES satellites (P2=MetOp2, P5=NOAA-15, P6=NOAA-16, P7=NOAA-17, P8=NOAA-18). The fluxes kept at the enhanced level for several hours. We analyze the peak fluxes in the FEE enhancements (time, local time, longitude, and L-shell). Positions of the satellite orbital planes provided a good coverage of the entire local time (LT) range: 9 - 21 LT (P2 and P7), 5 - 17 LT (P5 and P6), and 2 - 14 LT (P8). The coverage allows determining the injection region with uncertainty of approximately 2 h. The first FEE enhancement was observed at ~1250 UT in Central Pacific at night time (2 LT), and the last (enhancement number F15) was detected at ~2310 UT near the western edge of SAA at day time (17 LT). As seen in Figure 2a,b, the FEE enhancements peak at minimal L-shells, i.e. at the equator. The fluxes decrease quickly with growing L. This pattern corresponds to a fast radial transport (injection) of electrons from the inner radiation belt. Note that pitch-angular scattering of electrons gives different profiles: the fluxes should be minimal at the equator and grow with L-shell.

It was shown statistically that electron deep injections into the forbidden zone occur in the midnight - morning sector (Suvorova, 2017). During typical geomagnetic disturbances, nighttime FEE enhancements are observed shortly after local injections and near an injection site, while subsequent FEE enhancements at daytime are already the result of azimuthal drift of electrons injected at nighttime. Hence, the nighttime (~2 LT) enhancements F1 and F4 of >30 keV electron fluxes indicate approximately the time of injection, respectively, at ~1250 and ~1430 UT or a little bit earlier. After 1530 UT, enhancements were observed at daytime (numbers F7, F9, and F11-15) and are therefore associated with drifting electrons.

All remaining enhancements F2, F3, F5, F6, F8 and F10 of >30 keV electron fluxes were observed in the early morning (5 LT) for a long time interval of ~4 h that lead us to suspect that the enhancements were observed near the injection site. Nevertheless, we examine the assumption about drift by comparing these enhancements with the injection time for numbers 1 and 4 in Table 1. For the enhancements F1 and F2, 30 keV electrons injected at 1250 UT must drift ~35.4° of longitude in order to reach the observing satellite P5. It takes ~112 min with the drift rate of 19°/h for 30 keV electrons at L~1.2. However, the observed time difference between F1 and F2 is only 25 min that is too short for drifting from the longitude of F1 to the longitude of F2. The enhancements F1 and F3 have the longitudinal difference of 26° for 1 h that is much larger than 19° produced by the drift of ~30 keV electrons. In case of higher energy electrons (e.g., ~50 keV), the flux should have decreased notably due to falling energy spectrum.

Likewise, one can infer that the enhancement F4 also did not result in the enhancements F5 and F6 and certainly not in the enhancements F8 and F10. Therefore, the specific longitudinal and local time distributions of the enhancements indicate multiple injections during about 4.5 h in the sector of 0 - 6 LT, and the injection region was confined within 3 h of local time over central and eastern Pacific. In general, these characteristic of injections are in well agreement with those found from the statistics (Suvorova, 2017).

2.2. Upstream Solar Wind Conditions

An intriguing aspect of these FEE injection events is that they occurred under quiet, nonstorm conditions, characterized by Dst/SYM-H ~ 0 nT and AE < 100 nT (see Figure 3). We examine solar wind parameters to search for drivers inducing such deep electron injections. We focus on a comparison between the solar wind parameters measured far upstream and near the bow shock and on their influence on the magnetospheric magnetic field during the period of interest. Global indices of geomagnetic activity and upstream solar wind from the OMNI database in GSM coordinates are shown in Figure 3.

As seen in Figure 3, the solar wind speed and density smoothly varied around averages of 400 km/s and 6 to 4 cm^{-3}, respectively, that resulted in gradual change of the dynamic pressure *P*d from 2 to 1 nPa. The interplanetary magnetic field (IMF) can be characterized as weakly disturbed by small-scale structures because of chaotic variations of the magnetic field components and discontinuities, particularly during the fist half of the day. Also, in this period, the Bz component was predominately positive. Later, there was a short interval from 1500 to 1800 UT, when IMF orientation was relatively steady with a continuous negative Bz of about -2 nT. The *AL* index increased from 16 to 18 UT with a peak of -250 nT. The 1 min *SYM-H* index was > -10 nT throughout the whole day, indicating there was no geomagnetic storm.

Overall, the OMNI magnetic and plasma parameters can be characterized as almost undisturbed in the period of the FEE enhancements from 1200 to 2300 UT. Obviously, the weak auroral activity at ~1700 UT could not result in extremely deep injections of the energetic electrons, which started much earlier, around 1300 UT. Whereas, looking on the PC index, which represents magnetic activity in the northern (PCN) and southern (PCS) polar caps (Troshichev et al., 1988), one can see a clear disturbance, particularly in the northern polar cap, in the period from 1300 to 1530 UT. But it's difficult to identify appropriate solar wind drivers for interpretation of this polar cap activity.

This raises the question of actual solar wind characteristics at the near-Earth location during the event. The FEE enhancement event under the nonstorm condition and mild, ordinary solar wind properties presents intriguing challenge to current understanding of the energetic particle injections, which usually are associated with intense substorm activity. From the characteristic PC-index behavior, we suspect the actual solar wind parameters affecting the magnetosphere may be different from those predicted by OMNI. Fortunately, the near-Earth THEMIS mission can provide necessary reliable information on upstream conditions.

2.3. THEMIS foreshock observations

During the time interval from 1200 to 1800 UT, the THEMIS-C satellite (TH-C) moved from the subsolar region (17.2, -0.3, -5.9 Re GSM) toward dusk (18.1, 3.4, -5.9 Re GSM) (see Figure 4). From the TH-C plasma and magnetic measurements (Figure 5), we infer that the probe was located upstream of the bow shock, whose average subsolar position was estimated as ~14.6 Re for *Pd*~1.5 nPa (Fairfield, 1971). Figure 5a shows measurements of the THEMIS-C/FGM fluxgate magnetometer in GSM coordinates with a time resolution of ~3 s (Auster et al., 2008) and the ion spectrograms from THEMIS-C/ESA plasma instrument (McFadden et al., 2008). The ion spectrogram clearly demonstrates that hot ions (~ 1 keV) are of the solar wind origin and magnitudes of magnetic field components correspond to IMF components in Figure 3. The magnetic field components measured in situ by TH-C are compared with those predicted by OMNI and shown in Figure 5b. Also, Figure 5c presents the IMF cone angles, between the IMF vector and the Earth-Sun line, for both magnetic data sets. In Figure 5d, dynamic pressure for OMNI, ACE and TH-C are compared.

We evaluate characteristics of the upstream solar wind structures actually affecting the magnetosphere during the period of the FEE enhancements. From 1100 UT to 1320 UT, three TH-C magnetic components demonstrated small-amplitude variations, and the Bz component had northward direction. During this time, there were discrepancies between magnetic components of the TH-C and OMNI data caused mostly by time shift of ~10-15 min, so that TH-C observed arrival of the solar wind structures at earlier time than that predicted by OMNI. With time correction, one can achieve better consistency in the two magnetic data sets except the difference in the Bx components about 1310 UT.

In Figure 5c, the OMNI cone angle dropped below 30° between 1330 and 1520 UT that corresponded to quasi-radial IMF orientation (IMF is almost along the Earth-Sun line), whereas cone angle variations detected by TH-C were very different from the OMNI data. After 1500 UT, the OMNI data do not match the TH-C observation any more, even with time correction. About ~1320 UT, ~1400 UT and after 1440 UT, the in-situ observation of THEMIS shows large-amplitude fluctuations with duration of tens of minutes in three magnetic components and cone angle (Figure 5a, c). The observed large magnetic fluctuations are ultralow-frequency (ULF) waves, and they are a typical signature of the upstream region of quasi-parallel bow shocks, so-called foreshock (e.g., Schwartz and Burgess, 1991). In addition, in the same time intervals, the plasma spectrogram shows enhancements of suprathermal ion fluxes with energy of >10 keV (upper panel in Figure 5a). This is another distinguishing signature of the foreshock, known as diffuse ion population, which is always observed together with the upstream ULF waves (Gosling et al., 1978; Paschmann et al., 1979). Hence, the upstream foreshock waves and diffuse ions observed by TH-C in the subsolar region are associated distinctly with a radial or quasi-radial IMF orientation in the undisturbed solar wind. Note, that the longest foreshock interval (1435 - 1550 UT) associated with the quasi-radial IMF orientation was observed by ~20 min later than that predicted by OMNI.

After 1520 UT, the prediction and in-situ data mismatch greatly. The TH-C satellite observed several IMF discontinuities and alternation between spiral and radial orientations of the IMF vector, while the OMNI magnetic field does not change the spiral orientation from 1520 to 1740 UT. The foreshock returned to the subsolar region periodically and more frequently in the interval 1600 - 1730 UT than in the earlier period 1320 - 1440 UT. This behavior indicates the transient subsolar foreshock.

Note, these two time intervals of frequent foreshock transitions differ in the Bz component: Bz > 0 at 1320 - 1440 UT and Bz < 0 at 1600-1700 UT. It's natural, that the southward Bz results in the weak auroral activity during the later interval. Nevertheless, the changing direction of IMF has the effect on the magnetic activity in the northern polar cap during the both interval (see the PC index in Figure 1).

Figure 5d demonstrates large difference in solar wind dynamic pressure acquired from the TH-C probe, the ACE upstream monitor and OMNI data. The ACE data are shifted by 60 min. In contrast to OMNI and ACE, TH-C observed strong fast fluctuations in the dynamic pressure during intervals of subsolar foreshock (see Figure 5c). Note that ACE shows in average a smaller pressure than OMNI predicts, and it is more close to the TH-C observations. The fluctuations in the TH-C measurements are characterized by pressure pulses, which exceed sometimes the dynamic pressure from ACE (e.g., at 1320-1330, 1350, 1420, 1440, 1530 and etc.). The pulses were originated from plasma density enhancements because the plasma velocity remained practically constant at that time (not shown). Similar foreshock phenomenon was described by Fairfield et al. (1990). Apparently, the foreshock pressure pulses were further transported by the solar wind to the magnetosheath and could affect the magnetopause. Similar foreshock pressure pulses and their compression effects in the magnetosphere-ionosphere were reported by Korotova et al. (2011).

2.4. Magnetospheric magnetic field perturbations

We use magnetic field and plasma measurements in the magnetosphere from the other three THEMIS probes and GOES-12, GOES-10 satellites in order to examine a magnetospheric response to the pressure pulses in the subsolar foreshock, which forms each time with arrival or departure of magnetic flux tubes with quasi-radial IMF orientation. Positions of the TH-B, TH-D, TH-E and GOES-12 satellites in the X-Y GSM plane for the period from 1200 to 1800 UT are shown in Figure 4. We used the model of Lin et al. (2010) to calculate magnetopause position. The OMNI data at 1600 UT are used as input data for the model. The GOES-12 and GOES-10 satellites moved from morning to noon (7 - 13 LT and 8-14 LT, respectively). The TH-E and TH-D probes moved outward from prenoon to postnoon, and the TH-B probe moved inward in the afternoon-dusk sectors.

Figure 6 shows variations of the Bz component measured by the TH-E, TH-D, and TH-B probes, the magnetic field strength at geosyncronous orbit (GOES-12, -10), the ion spectrogram from the TH-D satellite and the SYM-H index from 1100 to 1800 UT. The THEMIS magnetic data were detrended using the Tsyganenko T04 geomagnetic field model (Tsyganenko and Sitnov, 2005) and IGRF-2005 model (see Figure 6b). The IGRF model describes the Earth's main magnetic field and the T04 model represents magnetic fields from the magnetospheric currents.

As seen in Figure 6 (a, e), characteristics of magnetic field and hot plasma indicate that three THEMIS probes were located inside the dayside magnetosphere, a region of strong magnetic field with the magnitude ranging from 40 to 150 nT and low-density of hot (>10 keV) ions. Three THEMIS probes and GOES observed significant perturbations in the magnetic field with increase/decrease of order of several to tens of nT (Figure 6 a-c). After 1600 UT, the largest (negative) amplitudes were observed by TH-D, which was mostly close to the magnetopause.

From 11 to 13 UT, one can see several increases of a few nT observed by GOES and/or THEMIS at ~1125, ~1200, ~1245 and ~1300 UT (Figure 6b). From 1300 to 1500 UT, there are a few characteristic decreases and increases with duration of 20-30 min observed by all probes. The magnetic field increases correspond to magnetospheric compressions, and the decreases are magnetospheric expansions (e.g., Dmitriev and Suvorova, 2012). Prominent magnetic "dimple-hump" structures are indicated by dashed lines (as 1, 2, and 3) and their peaks are listed in Table 2. We select peak-to-peak amplitudes exceeded ~5 nT in the GOES data (Figure 6c). The dimple-hump structures show the largest amplitudes up to 15 nT in THEMIS data (Figure 6b).

After 1600 UT, the TH-D probe observed fast magnetic variations. At that time, the probe was approaching the magnetopause and moving ahead of the TH-E probe (see Figure 4). Note, that the fast magnetic fluctuations are not always seen in SYM-H index because of a low time resolution (1 min). Figure 6e presents the ion spectrogram from TH-D. One can see several short-time intrusions of dense and cold plasma with spectrum typical for the magnetosheath. Moreover, at ~1700 and 1710 UT, the magnetospheric field measured by TH-D with positive Bz suddenly overturned to negative Bz for a moment that indicated a magnetosheath encounter. Time moments of peaks in the magnetosheath plasma pressure are indicated by lines 4-10 in Figure 6 and listed in Table 2.

As seen in Figures 6b-d, THEMIS magnetic observations well correlate with magnetic field variation observed by GOES-12,-10 in the whole interval. Time of some magnetic peaks coincides well with accuracy of 1 min (e.g., at ~1200, 1300 and 1420 UT), while others demonstrate various delays of 2 - 6 min between different satellites (see Table 2). In Table 2, we also list foreshock pulses related to the magnetic peaks observed in the magnetosphere (see Figure 5d). Comparing the time moments of magnetic peaks and foreshock pressure pulses, we found that the latter often preceded the first ones by one to few minutes.

As we have found, the magnetic variations associated with expansion-compression effects could not be caused by the pristine solar wind pressure variations, which were gradual and small during the interval (see Figures 3 and 5). The magnetic perturbations can be related to the foreshock pressure pulses. Unfortunately, THEMIS was not located in the magnetosheath from 1200 to 1600 UT, but an analysis of the later interval (1600-1800 UT) can provide important information about penetration of the foreshock pressure pulses through the magnetosheath.

2.5. Magnetosheath plasma jets interacting with the magnetopause

Figure 7 shows the magnetic field and plasma parameters observed by TH-D, TH-E and TH-C during the interval 1530-1800 UT. In addition, magnetic measurements from GOES 12, IMF cone angle from ACE and TH-C, and dynamic pressure from TH-C are shown. After 1530 UT, the TH-D and TH-E probes have observed magnetic field increases associated with the compression effect (Figure 7d). After 1600 UT, TH-D was approaching the magnetopause and started observing occasionally magnetosheath plasma in the magnetosphere, as seen in the ion spectrogram (e.g., lines #4 – 7 and 10, Figures 7b). After 1700 UT, the probe twice encountered the magnetosheath region as indicated by lines #8 and #9. The magnetosheath plasma can be recognized as dense and cold (<1 keV) ion population.

As seen in Figure 7 (panels b and d), not all magnetic peaks are accompanied by plasma penetrations. During the interval, the outermost probe TH-C observed occasionally the foreshock phenomena, such as diffuse ions (≥10 keV), ULF waves and pressure pulses (panels a, e, f). As one can see, most of the magnetic peaks at panel d and/or magnetosheath ions at panel b were preceded by the foreshock pressure pulses within 1-5 min (panel f), for example at ~1549, ~1611, ~1625 UT and etc. (see Table 2). There are exceptions for plasma penetrations #6 at 1648 UT and #7 at 1651:30 UT. Note that those events were preceded by IMF discontinuities as one can find in rotation of the cone angle (panel e) at 1645 and 1650 UT, respectively.

Figure 8 shows characteristics of magnetosheath plasma in details for three intervals 1600-1630, 1630-1700, and 1658-1728 UT. Since plasma charge neutrality means equal density of ions and electrons, Figure 8 presents parameters of the ion component only (panels a-d). Total pressure (*P*tot) and density (*D*) of the solar wind plasma measured far upstream by the ACE monitor are also shown for comparison in panels (b, c). The time period from 1600 to 1630 UT is shown in panels (a1-g1). The probes TH-D and TH-E observed magnetic field variation as a specific dimple-hump pattern from 1609 to 1615 UT (panels f1, g1), similar to the variations indicated by lines #1 - #3 in the earlier interval (see Figure 6). This magnetic variation is preceded by the dimple-hump variation in the foreshock pressure as observed by TH-C at 1607 to 1611 UT (see Figure 7f).

The dimple-hump variations are followed by penetration of the magnetosheath ions into the magnetosphere as observed by TH-D at 1614 to 1616 UT (#4 in Table 2). At 1614 - 1616 UT, TH-D was located in the magnetosphere but it observed cold ions (~100 eV - 3 keV) and electrons (<1 keV, not shown) of the magnetosheath origin (Figure 8, panel a1). The plasma has maximal speed of >200 km/s and high density of 3-9 cm^{-3} that result in the high total pressure of 1.5 - 1.8 nPa (panels b1-d1). Its dynamical characteristics distinctly exceed the solar wind parameters with density of 4 - 5 cm^{-3} and total pressure of ~1.1 nPa (panels b1, c1). The internal structure of plasma forms 3 prominent pressure pulses between 16:14:50 and 16:16:00 UT, a central pulse is dominated by magnetic component (panel f1) and two lateral pulses are dominated by dense plasma components (panel c1). Two plasma density enhancements produced a diamagnetic effect seen as a characteristic decrease of magnetic field (panel f1). At the outer edge of the plasma structure, the anti-sunward velocity (Vx < 0) reached high value of -100 km/s, indicating that the local plasma flow struck and interacted with the magnetopause (panel d1). The Vz component demonstrates a maximal value in southward direction (-200 km/s). Three rotated velocity components Vx, Vy and Vz indicate that vortex-like plasma structure propagated along the magnetopause toward south and dusk. This dense and high-speed plasma structure is analogous to the large-scale magnetosheath plasma jet studied by Dmitriev and Suvorova (2012). The jets are defined as intense localized fast ion fluxes whose kinetic energy density is several times higher than that in the upstream solar wind and duration is longer than 30 sec (Dmitriev and Suvorova, 2015; Plaschke et al., 2018).

Panels (a2-g2) in Figure 8 show magnetosheath plasma penetrations #5 - #7 during the time period from 1630 to 1700 UT. The plasma structures #5 and #6 (panel a2) have a short duration and are characterized by extremely high density of 16 and 12 cm^{-3}, respectively, that well explain the compression effects in magnetic measurements from TH-E and TH-D (panels f2, g2). Prolonged plasma structure #7 has lower density of 4 - 9 cm^{-3} and did not produce a notable compression in accordance with to TH-E magnetic measurements (panel g2). Note that the structure #5 was preceded by a foreshock pulse observed at ~1637 UT while there were no foreshock pulses before the structures #6 and #7.

It is important that inside each plasma structure, we reveal a dense plasma core, which is characterized by enhanced speed of ~150 or ~220 km/s with a dominant Vz component (negative or positive). These parameters, typical for plasma jets, formed pressure of high magnitude, which exceeded the upstream solar wind pressure by 50-80 % (panel b2). The magnetosheath plasma jets interacted with the magnetopause that resulted in penetration of the magnetosheath plasma into the magnetosphere (Dmitriev and Suvorova, 2015). The amount of penetrated plasma can be comparable with estimates of the total amount of plasma entering the dayside magnetosphere (Sibeck, 1999).

During the last period at 1658 - 1728 UT shown in panels (a3-g3), we have an excellent opportunity to examine plasma parameters in the magnetosheath region adjacent to the magnetopause. Panels (a3-f3) show two cases of magnetopause distortions followed by short intervals of the magnetosheath from ~1700 to 1701 UT and from 1711 to ~1715 UT. The TH-D probe at distance of ~10.8 Re and ~13 LT suddenly crossed the magnetopause and moved into the magnetosheath, where Bz < 0 (panel f3). Plasma in both magnetosheath intervals has extremely high density (~20 cm^{-3}) and high velocity (≤ 200 km/s). In the magnetosheath, one can see local pressure pulses around ~1700 UT and ~1712 UT (lines #8 and 9). For #9 case, TH-E observed a small shallow hump of the magnetic field of a few nT between two depletions at 1707 and 1715 UT (panel g3). The last event (#10) shown in Figure 8c is a short penetration of magnetosheath plasma accompanied by a small perturbation in the magnetospheric field observed at ~1724-1725 UT (panels e3, f3). The density and pressure of this structure did not exceed the solar wind parameters (panel b3-d3). Note that foreshock pressure pulses preceded by few minutes the magnetic peaks and plasma structures #8, #9 and #10 as seen in Figure 7.

Thus, we found typical characteristics of dense and fast plasma jets in all intrusions of the magnetosheath plasma into the magnetosphere and in the magnetosheath itself. Most of the penetrating magnetosheath jets correspond to the foreshock pressure pulses. All jet-related plasma structures caused local compression effects at the dayside. This finding raises further an interesting question about spatial distribution of geomagnetic field response to the impact of foreshock pressure pulses on the dayside magnetopause during very quiet geomagnetic conditions at 1300 - 1600 UT.

2.6. Global ground-based magnetic variations

The global dynamics of geomagnetic field perturbations was studied using 1-min magnetic data provided by an INTERMAGNET of ground magnetometers (http://www.intermagnet.org/index-eng.php). We used magnetic stations located at geomagnetic latitudes below ~60° (Table 3), where a significant effect of different propagation time of MHD waves in the magnetosphere was almost hidden at 1 min resolution. We grouped magnetic stations in meridional and latitudinal chains.

Figure 9 presents relative variations of horizontal (H) component measured at equatorial and low geomagnetic latitudes (from 0° to ~20°) in the interval from 1100 to 1600 UT. The stations are arranged in local time from morning to postmidnight. The GOES-12 and detrened TH-D magnetic data are shown at bottom. Four magnetic field pulses of different amplitudes are seen around ~1200, ~1335-1345, ~1422-1430 and ~1545-1550 UT practically at all stations. The last three pulses correspond to those selected from THEMIS data at ~1334, ~1421 and 1547-1550 UT (#1 - #3, see also Table 2). Moreover, one can see the same pattern of magnetic variation "dimple-hump" in both ground-based and satellite observations. An earlier magnetic pulse of a smaller amplitude at ~1200 UT is also seen in the GOES-12 and TH-D data.

It is interesting, that the magnetic pulse at 1200 UT is simultaneously (within the accuracy of ~1 min resolution) observed in all local time sectors. However, the other three enhancements were observed in different LT sectors at slightly different time. The time difference varies from ~2 min to ~10 min. The time delay depends on the time moment when a jet interacts with the magnetopause in a given latitude-longitude sector (Dmitriev and Suvorova, 2012).

We draw attention to the fact that low-latitude HON and PPT stations, which were located in the predawn sector (2-5 LT) from 1300 to 1500 UT, demonstrate the best coincidence (with a delay of ~1 min) of magnetic peaks #1 and #2 with those observed by THEMIS near noon. Nighttime and daytime stations (PHU, GZH, KNY, KDU, GUA, MBO, ASC, TSU, BNG, AAE, ABG) observed these peaks with ~3 - 5 min delay. The longest delay (~7 min) for pulses #1 and #2 is found at morning/prenoon stations KOU and VSS (~9 - 11 LT).

As we have showed above, the FEE injections (F1 - F6 in Table 1) occur from ~2 to 5 LT. So, we present meridional chains of stations in the predawn and midnight sectors (Figure 10). All magnetic pulses are well recognized from 0° to 60° of geomagnetic latitude. In midnight and predawn sectors, the magnetic pulse at ~1200 UT peaks practically simultaneously everywhere. Magnetic peak #1 around ~1333 UT was delayed by ~7 min at midlatitudes (30°-60°) in the midnight sector (left panel) and by ~5 min in the predawn sector (right panel). The pulse #2 shows a smaller delay (~3 min) at midlatitudes. The magnetic peak #3 at most stations in both sectors is observed around ~1545 UT, that is 2 min earlier than at TH-E and 1 min later than at GOES (see Table 2).

Thus, the ground-based magnetic observations at low and middle latitudes demonstrate similarity in the magnetic variations of "dimple-hump" pattern with the satellite observations in the dayside magnetosphere. It should be noted that the magnetic peaks are not regular and are characterized by periodicities of tens of minutes that distinct them from magnetospheric quasi-periodic ULF waves with periods 1 – 600 s. Hence, the variations observed in the geomagnetic field should result from pressure pulses of the subsolar foreshock and/or magnetosheath origin.

3. Discussion and Summary

In this work, using NOAA/POES and THEMIS satellites we investigated an unusual case of deep injections of >30 keV electrons at L< 1.2 and corresponding upstream conditions during quiet day on August 1, 2008. Strong FEE enhancements with intensity of up to ~10^5 (cm^2 s $sr)^{-1}$ were observed by POES above central and eastern Pacific for a long time from ~1300 to 2300 UT. With analysis of longitudinal and local time distributions of the enhancements we identified a series of nightside injections occurred in the sector of 2 - 5 LT during the period from ~1300 to ~1700 UT (Figure 2). We found that the first 6 injections (Table 1) occurred before intensification of auroral activity started at 1600 UT, and hence, cannot be related to the substorm. Two injections occurred during the interval of weak auroral activity at 1600 - 1800 UT.

We found that from 11 to 18 UT the magnetosphere was not completely quiet. Prominent magnetic variations on the dayside were observed by THEMIS and GOES satellites and by ground-based magnetometers from INTERMAGNET network. The variations correspond to magnetospheric expansions and compressions. Comparative analysis of the THEMIS, OMNI and ACE data showed that the geomagnetic perturbations were not driven by the dynamic pressure of the pristine solar wind. Note that significant discrepancies between the OMNI data and THEMIS near-earth observations under quasi-radial IMF were reported frequently (e.g., McPherron et al., 2013; Suvorova and Dmitriev, 2016). THEMIS observations show firmly that geomagnetic perturbations were rather related to changes in the IMF cone angle and pressure pulses in the subsolar foreshock.

We demonstrated that in the magnetosheath, foreshock pressure pulses could be transformed to fast and dense magnetosheath streams, so-called jets. We found that 5 out of 7 magnetosheath jets were preceded by the foreshock pressure pulses. These results support well the previous findings that the plasma jets are typical consequence of the foreshock dynamics and variations in the IMF orientation (e.g., Fairfield et al., 1990; Lin et al., 1996; Archer et al., 2012; Dmitriev and Suvorova, 2012; 2015; Plaschke et al., 2018). In addition, similar effects of the foreshock pressure pulses and magnetosheath jets in the magnetosphere were reported (e.g., Sibeck and Korotova, 1996; Korotova et al., 2011; Heitala et al., 2012).

In the present case, the amplitude of magnetic variations was not very high: from a few nT at ground to 15 nT at THEMIS. It should be noted that such magnetic perturbations are too weak to produce deep injections of >30 keV electrons below the radiation belt. On the other hand, the interaction of jets with the magnetopause can result also in penetration of the magnetosheath plasma inside the dayside magnetosphere (Dmitriev and Suvorova et al., 2012, 2015). Precipitation of hot magnetospheath and/or magnetospheric plasma into the dayside high-latitude ionosphere can cause intensification of dayside aurorae. Vorobjev et al (2001) analyzed dayside auroral transient events at latitudes equatorward of the auroral oval (below 76º). They found that the dayside aurora brightening was related to localized magnetospheric compressions driven by abrupt changes in the foreshock (but not by variations in the solar wind dynamic pressure). Recent comprehensive and statistical studies present observations of dayside aurora brightening related to localized magnetopause indentations (Han et al., 2018) and caused by magnetosheath high-speed jets (Wang et al., 2018). Additionally, Han et al. (2016) provided direct evidence that the source of precipitating particles in the dayside aurorae was the magnetosheath plasma (sometimes mixed with magnetospheric plasma). Thus, these studies showed that the jet impact is responsible for transient dayside aurora, which provides enhancements in conductivity of the auroral ionosphere on the dayside.

In order to find signatures of particle precipitations at high latitudes we conducted an additional analysis of hot plasma precipitations in the auroral region at *L*-shells from 7 to 15 during the time of interest. The energy fluxes of hot plasma (from 50 eV to 10 keV) were measured by POES/TED plasma spectrometer. Figure 11 demonstrates magnetic observations of THEMIS and GOES, and POES observations of the energy fluxes of auroral precipitations and FEE injections. We consider intense precipitations with the threshold of 0.5 (erg cm^{-2} s^{-1}), which is several times higher than the background. One can see that from 11 to 16 UT, the hot plasma precipitated mainly on the dayside (12 – 16 LT) while after 16 UT, the precipitations occurred practically at all local times both on the day and night sides.

The first FEE injection (F1) at ~1250 UT was preceded by several geomagnetic pulses observed by GOES-12 and TH-D. The pulses were not very prominent because at that time, GOES-12 was located in the morning sector and TH-D was inside the geosynchronous orbit. One can see that some of pulses were accompanied by dayside auroral precipitations of the hot plasma. Note that POES satellites have 100 min orbital period and, hence, they can miss some of localized precipitations. On the other hand, when a jet hits the magnetopause, the magnetosheath plasma is not necessarily penetrating into the dayside magnetosphere and, hence, precipitating at high latitudes [*Dmitriev and Suvorova*, 2015]. Nevertheless, in Figure 11, we find two cases of geomagnetic pulses followed by intense dayside precipitations of the hot plasma at 1105 UT and 1145 UT.

We can propose that the dayside precipitations at high latitudes are associated with the effect of jets piercing the magnetopause. The average flux of jet-related penetrating plasma was estimated as 3 10^8 $(cm^2\ s)^{-1}$ (Dmitriev and Suvorova, 2015). This particle flux corresponds well to the energy fluxes >0.5 erg cm^{-2} s^{-1} of precipitating ions with energy of ~1 keV measured by POES/TED at high latitudes (see Figure 11). Hence, the jet-related magnetosheath plasma can produce significant additional ionization and increase conductivity of the high-latitude ionosphere on the dayside.

The precipitations of hot plasma to the dayside ionosphere at high latitudes produce a local increase of the ionospheric conductivity. An enhancement of electric currents in the dayside ionosphere should in turn promote generation of transient localized electric fields on the nightside and especially in the postmidnight sector, where the conductivity is weak. We hypothesize that the induced nightside electric field might penetrate from high to low latitudes (very low L shells) and results in ExB drift of electrons to lower L-shells.

The drift takes a certain time dT to transport electrons from the inner radiation belt edge (at *L*-shell $L_1 = 1.2$) to the heights of ~900 km (L-shell $L_2 = 1.1$~1.15):

$$dT(s)= 6380 * (L_1 – L_2)/V_{DE} \qquad (1)$$

where the *ExB* drift velocity is determined as

$$V_{DE} = 0.032 * L^3 * E, \qquad (2)$$

where L the average L-shell in the first approach and E is azimuthal electric field in mV/m. From equations (1) and (2), we estimate that the earthward drift of energetic electron across the magnetic field lines from $L = 1.2$ to $L = 1.1$ takes up to 40 min under local electric field of ~5 mV/m. Note that E ~ 5 mV/m was obtained in simulations of energetic electron injections at $L <$ 1.3 [*Selesnick et al.*, 2016].

In our case of non-storm conditions, it is hard to imagine that the strong azimuthal *E* can persist for so long time. Previously, simulations by Su et al. (2016) have showed that it is not necessary for electrons to be transported earthward all the way during a single injection. Hence, we can consider a multi-step radial transport produced by a number of short pulses of *E*. In this case, the drift from *L*=1.2 to *L*=1.1 requires two or more pulses of ~10 min duration that is comparable with the duration of jet-related disturbances. The multi-step process is limited by the time, during which a particle stays in the region of injection. The >30 keV electrons have a long period of azimuthal drift and, thus, they can stay in the region for hours. In contrast, the >100 keV electrons with the azimuthal period of ~6 h leave quickly the injection region and, thus, do not have enough time to penetrate to the forbidden zone. This effect can explain the absence of high-energy electrons in the FEE enhancements presented.

In this scenario, the first FEE injection requires a long time (~hour and longer) and several pulses of *E* in order to transport energetic electrons from undisturbed edge of the inner radiation belt to *L*~1.1. Then, >30 keV electrons populate *L*-shells from 1.15 to 1.1 that makes possible to transport electrons to 900 km heights for a short time of ~10 min by one pulse of strong *E*. The latter pattern is applicable for the FEE injection F2. As one can see in Figure 11, each FEE injection after 13 UT is preceded within <30 min by intense auroral precipitations of the hot plasma.

Summarizing, we can propose the following interpretation of the observations:

1. During quiet solar wind and geomagnetic conditions, the magnetosphere can be substantially disturbed due to transient subsolar foreshock under radial IMF.

2. Subsolar foreshock pressure pulses and IMF discontinuities result in generation of fast and dense plasma jets in the magnetosheath.

3. The jets interaction with the dayside magnetopause produces two distinct features in the magnetosphere: geomagnetic pulses due to the compression and magnetosheath plasma penetration.

4. Precipitations of the magnetosheath plasma fluxes of the order of 1 (erg cm^{-2} s^{-1}) to the dayside high-latitude ionosphere should result in a local increase of the ionospheric conductivity and an enhancement of electric currents in the dayside ionosphere. The latter should promote generation of transient localized electric fields on the nightside and especially in the postmidnight sector.

5. We hypothesize that the induced nightside electric field might penetrate from high to low latitudes (very low L shells).

6. Quantitative estimations show that the electric field of ~5 mV/m can provide the fast *ExB* transport of electrons from the inner radiation belt at $L < 1.5$ to lower heights ($L < 1.2$). The transport of inner belt electrons is responsible for the observed FEE enhancements.

It should be noted that most favorable conditions for FEE enhancements (and, presumably, for penetration of localized electric fields) arise in the period from May to September independently on geomagnetic activity level (Suvorova, 2017) Similar asymmetry in the dayside auroral conductivity was also shown by Sibeck et al., (1996). Our case event on 1 August 2008 corresponds well to these favorable conditions. Further observations of jet-related magnetospheric - ionospheric phenomena are required to confirm this scenario.

Another serious problem is the generation/penetration of electric fields in the inner magnetosphere, which is far from complete understanding. At the present time, there are no models predicting strong electric fields in the inner radiation belt and below. As conjugate observations of penetrating transient electric fields are still unavailable for such cases of anomalous particle transport, the exact mechanism of deep electron injections cannot as yet be fully determined. In this sense, the scenario suggested here requires further experimental studies and *in situ* observations of electric fields at *L*-shells from 1.1 to 2.

Data availability.

CDAWEB (https://cdaweb.gsfc.nasa.gov/index.html) provide the NOAA/POES energetic particle data, THEMIS magnetic and plasma data, OMNI and ACE solar wind data. Kyoto World Data Center for Geomagnetism (http://wdc.kugi.kyoto-u.ac.jp/index.html) provides the geomagnetic indices. The ground magnetogram were collected from INTERMAGNET network (www.intermagnet.org).

Author contributions.

AS, AD and VP processed and analyzed experimental data on energetic particles, magnetic fields and plasma. AS found the event and designed the study. AD developed the software for treatment of the satellite data. VP analyzed ground-based magnetograms and contributed to discussion of results. AS and AD performed the whole analysis of the data, prepared figures and wrote the paper, as well as answered the referees during the evaluation process.

Competing interests.

The authors declare that they have no conflict of interest.

Acknowledgements

We thank the THEMIS team for magnetic and plasma data provided. We thank the national institutes that support magnetic observatories from INTERMAGNET. We thank Prof. O.Troshichev for providing the PC-index.

Financial support.

This research was supported by grant MOST 106-2811-M-008-050 and MOST 106-2111-M-008-030-MY3 to National Central University.

References

Archer, M. O., Horbury, T. S., and Eastwood, J. P.: Magnetosheath pressure pulses: Generation downstream of the bow shock from solar wind discontinuities, J. Geophys. Res., 117, A05228, https://doi.org/10.1029/2011JA017468, 2012.

Asikainen, T., and Mursula, K.: Filling the South Atlantic anomaly by energetic electrons during a great magnetic storm, Geophys. Res. Lett., 32, L16102, https://doi.org/10.1029/ 2005GL023634, 2005.

Auster, H. U., Glassmeier, K. H., Magnes,W., Aydogar, O., Baumjohann, W., Constantinescu, D., Fischer, D., Fornacon, K. H., Georgescu, E., Harvey, P., Hillenmaier, O., Kroth, R., Ludlam, M., Narita, Y., Nakamura, R., Okrafka, K., Plaschke, F., Richter, I., Schwarzl, H., Stoll, B., Valavanoglou, A., Wiedemann, M.: The THEMIS fluxgate magnetometer, Space Sci. Rev., 141(1–4), 235– 264, https://doi.org/10.1007/s11214-008-9365-9, 2008.

Dmitriev, A. V., and Suvorova, A. V.: Traveling magnetopause distortion related to a large-scale magnetosheath plasma jet: THEMIS and ground-based observations, J. Geophys. Res., 117, A08217, https://doi.org/10.1029/2011JA016861, 2012.

Dmitriev, A. V., and Suvorova, A. V.: Large-scale jets in the magnetosheath and plasma penetration across the magnetopause: THEMIS observations, J. Geophys. Res. Space Physics, 120, 4423–4437, https://doi.org/10.1002/ 2014JA020953, 2015.

Dmitriev, A. V., and Yeh, H.-C.: Storm-time ionization enhancements at the topside low-latitude ionosphere, Ann. Geophys., 26, 867-876, 2008.

Dmitriev, A. V., Suvorova, A.V., Klimenko, M. V., Klimenko, V. V., Ratovsky, K. G., Rakhmatulin, R. A., and Parkhomov, V. A.: Predictable and unpredictable ionospheric disturbances during St. Patrick's Day magnetic storms of 2013 and 2015 and on 8-9 March 2008, J. Geophys. Res.: Space Physics, 122, 2398-2432, https://doi.org/10.1002/2016JA023260, (2017).

Glocer, A., Fok, M.-C., Nagai, T., Tóth, G., Guild, T., and Blake, J.: Rapid rebuilding of the outer radiation belt, J. Geophys. Res., 116, A09213, https://doi.org/10.1029/2011JA016516, 2011.

Gosling, J. T., Asbridge, J. R., Bame, S. J., Paschmann, G., and Sckopke, N.: Observations of two distinct populations of bow shock ions in the upstream solar wind, J. Geophys. Res., 5, 957–960, 1978.

Evans, D. S., and Greer, M. S.: Polar Orbiting Environmental Satellite Space Environment Monitor: 2. Instrument descriptions and archive data documentation. Tech. Memo. version 1.4, NOAA Space Environ. Lab., Boulder, Colo., 2004.

Fairfield, D.: Average and unusual locations of the Earth's magnetopause and bow shock, J. Geophys. Res., 76(28),6700-6716, 1971.

Fairfield, D. H., W. Baumjohann, G. Paschmann, H. Luehr, and D. G. Sibeck (1990), Upstream pressure variations associated with the bow shock and their effects on the magnetosphere, *J. Geophys. Res.*, *78*, 3731-3744.

Han, D.-S., Nishimura, Y., Lyons, L. R., Hu, H.Q., and Yang, H. G.: Throat aurora: The ionospheric signature of magnetosheath particles penetrating into the magnetosphere, Geophysical Research Letters, 43, 1819-1827, https://doi.org/10.1002/2016GL068181, 2016.

Han, D.-S., Liu, J.-J., Chen, X.-C., Xu, T., Li, B., Hu, Z.-J., Hu, H. Q., Yang, H. G., Fuselier, S. A., and Pollock, C.J.: Direct evidence for throat aurora being the ionospheric signature of magnetopause transient and reflecting localized magnetopause indentations. J. Geophys. Res. Space Physics, 123, 2658-2667, https://doi.org/10.1002/2017JA024945, 2018.

Hietala H., N. Partamies, T. V. Laitinen, et al.: Supersonic subsolar magnetosheath jets and their effect: from the solar wind to the ionospheric convection, Ann. Geophys., 30, 33-48, 2012.

Korotova, G. I., D. G. Sibeck, A. Weatherwax, V. Angelopoulos, and V. Styazhkin (2011), THEMIS observations of a transient event at the magnetopause, J. Geophys. Res., 116, A07224, doi:10.1029/2011JA016606.

Krasovskii, V. I., Shklovski, I. S., Galperin, Yu. I., Svetlitskii, E. M., Kushnir, Yu. M., and Bordovskii, G. A.: The detection of electrons with energies of approximately l0 keV in the upper atmosphere (in Russian). Iskusstvennye Sputniki Zemli, 6, 113-126, (English translation: Planet. Space Sci., 9, 27-40, 1962), 1961.

Lejosne, S., and Mozer, F. S.: Typical values of the electric drift E × B/B2 in the inner radiation belt and slot region as determined from Van Allen Probe measurements, J. Geophys. Res. Space Physics, 121, 12,014–12,024, https://doi.org/10.1002/2016JA023613, 2016.

Lin, Y., Lee, L. C., and Yan, M.: Generation of dynamic pressure pulses downstream of the bow shock by variations in the interplanetary magnetic field orientation, J. Geophys. Res., 101, 479–493, 1996.

Lin, R. L., Zhang, X. X. , Liu, S. Q., Wang, Y. L., and Gong, J. C.: A three-dimensional asymmetric magnetopause model. J. Geophys. Res., 115, A04207, https://doi.org/10.1029/2009JA014235, 2010.

Matsui, H., Torbert, R. B., Spence, H. E., Khotyaintsev, Yu. V., and Lindqvist, P.-A.: Revision of empirical electric field modeling in the inner magnetosphere using Cluster data, J. Geophys. Res. Space Physics, 118, 4119–4134, https://doi.org/10.1002/jgra.50373, 2013.

McFadden, J. P., Carlson, C. W., Larson, D., Ludlam, M., Abiad, R., Elliott, B., Turin, P., Marckwordt, M., and Angelopoulos,V.: The THEMIS ESA plasma instrument and in-flight calibration, Space Sci. Rev., 141, 277–302, https://doi.org/10.1007/s11214-008-9440-2, 2008.

McPherron, R. L., Baker, D. N., Pulkkinen, T. I, Hsu,T. S., Kissinger, J., and Chu, X.: Changes in solar wind–magnetosphere coupling with solar cycle, season, and time relative to stream interface, J. Atmos. Sol. Terr. Phys., 99, 1-13, https://doi.org/10.1016/j.jastp.2012.09.003, 2013.

Park J., Min, K. W., Summers, D., Hwang, J., Kim, H. J., Horne, R. B., Kirsch, P., Yumoto, K., Uozumi, T., Lühr, H., and Green, J.: Non-stormtime injection of energetic particles into the slot region between Earth's inner and outer electron radiation belts as observed by STSAT-1 and NOAA-POES, Geophys. Res. Lett., 37, L16102, https://doi.org/10.1029/2010GL043989, 2010.

Paschmann, G., Sckopke, N., Bame, N., Gosling, J.T., Russell, C.T., and Greenstadt, E.W.: Association of low-frequancy waves with suprathermal ions in the upstream solar wind, Geophys. Res. Lett., 6, 209-212, 1979.

Pfitzer, K. A., and Winckler, J. R.: Experimental observation of a large addition to the electron inner radiation belt after a solar flare event, J. Geophys. Res., 73(17), 5792–5797, 1968.

Plaschke, F., Hietala, H., Archer M., et al.: Jets downstream of collisioness shocks, Space Science Review, 214:81, https://doi.org/10.1007/s11214-018-0516-3, 2018

Rowland, D. E., and Wygant, J. R.: Dependence of the large-scale, inner magnetospheric electric field on geomagnetic activity, J. Geophys. Res., 103(A7), 14959-24964, 1998.

Savenko, I. A., Shavrin, P. I., and Pisarenko, N. F.: Soft particle radiation at an altitude of 320 km in the latitudes near the equator (in russian). Iskusstvennye Sputniki Zemli, 13, 75-80 (English translation: Planet. Space Sci., 11, 431-436, 1963), 1962.

Schwartz, S. J., and Burgess, D.: Quasi-parallel shocks: A patchwork of three-dimensional structures, Geophys. Res. Lett., 18, 373-376, 1991.

Selesnick, R. S., Su, Y.-J., and Blake, J. B.: Control of the innermost electron radiation belt by large-scale electric fields, J. Geophys. Res. Space Physics, 121, 8417–8427, https://doi.org/10.1002/2016JA022973, 2016.

Sibeck, D. G.: Plasma transfer processes at the magnetopause, Space Sci. Rev., 88, 207–283, https://doi.org/10.1023/a:1005255801425, 1999.

Sibeck D.G., & G.I. Korotova (1996), Occurrence patterns for transient magnetic field signatures at high latitudes. J. Geophys. Res. 101, 13413–13428.

Sibeck, D., Greenwald R.A., Bristow W.A., and Korotova G.I.: Concerning possible effects of ionospheric conductivity upon the occurrence patterns of impulsive events in high-latitude ground magnetograms, *J. Geophys. Res.*, 101(A6), 13407– 13412, doi:10.1029/96JA00072., 1996

Su, Y-J, Selesnick, R. S., and Blake J. B.: Formation of the inner electron radiation belt by enhanced large-scale electric fields, J. Geophys. Res. Space Physics, 121, 8508–8522, https://doi.org/10.1002/2016JA022881, 2016.

Suvorova, A. V., and Dmitriev, A. V.: Radiation aspects of geomagnetic storm impact below the radiation belt, In V. P. Banks (Ed.), Cyclonic and Geomagnetic Storms: Predicting Factors, Formation and Environmental Impacts, (pp. 19-75), New York: NOVA Science Publishers, Inc., 2015.

Suvorova, A. V., and Dmitriev, A. V.: On magnetopause inflation under radial IMF, Adv. Space Res., 58, 249-256, 2016.

Suvorova, A. V., Dmitriev, A.V., and Tsai, L.-C.: On relation between mid-latitude ionospheric ionization and quasi-trapped energetic electrons during 15 December 2006 magnetic storm, Planet. Space Sci., 60, 363-369, https://doi.org/10.1016/j.pss.2011.11.001, 2012.

Suvorova, A. V., Dmitriev, A. V., Tsai, L.-C., Kunitsyn, V. E., Andreeva, E. S., Nesterov, I. A., and Lazutin, L. L.: TEC evidence for near-equatorial energy deposition by 30 keV electrons in the topside ionosphere, J. Geophys. Res., 118, 4672–4695, https://doi.org/10.1002/jgra.50439, 2013.

Suvorova, A. V., Huang, C.-M., Matsumoto, H., Dmitriev, A. V., Kunitsyn, V. E., Andreeva, E. S., Nesterov, I. A., and Tsai, L.-C.: Low-latitude ionospheric effects of energetic electrons during a recurrent magnetic storm, J. Geophys. Res. Space Physics, 119, 9283-9303, https://doi.org/10.1002/2014JA020349, 2014.

Suvorova, A. V., Huang, C.-M., Dmitriev, A. V., Kunitsyn, V. E., Andreeva, E. S., Nesterov, I. A., Klimenko, M. V., Klimenko, V. V., and Tumanova, Yu. S.: Effects of ionizing energetic electrons and plasma transport in the ionosphere during the initial phase of the December 2006 magnetic storm, J. Geophys Res.: Space Physics, 121, 5880-5896, https://doi.org/10.1002/2016JA022622, 2016.

Suvorova, A.V.: Flux enhancements of >30 keV electrons at low drift shells L <1.2 during last solar cycles, J. Geophys Res.: Space Physics, 122, 12274-12287, https://doi.org/10.1002/2017JA024556, 2017.

Tadokoro, H., Tsuchiya, F., Miyoshi, Y., Misawa, H., Morioka, A., and Evans, D. S.: Electron flux enhancement in the inner radiation belt during moderate magnetic storms, Ann. Geophys., 25, 1359-1364, 2007.

Tsyganenko, N. A., and Sitnov, M. I.: Modeling the dynamics of the inner magnetosphere during strong geomagnetic storms, *J. Geophys. Res.*, 110, A03208, https://doi.org/10.1029/2004JA010798, 2005.

Troshichev, O. A., Andrezen, V. G., Vennerstrøm, S., and Friis-Christensen, E.: Magnetic activity in the polar cap – A new index, Planet. Space Sci., 36(11), 1095–1102, 1988.

Turner, D. L., Claudepierre, S. G., Fennell, J. F., O’Brien, T. P., Blake, J. B., Lemon, C., Gkioulidou, M., Takahashi, K., Reeves, G. D., Thaller, S., Breneman, A., Wygant, J. R., Li, W., Runov, A., and Angelopoulos, V.: Energetic electron injections deep into the inner magnetosphere associated with substorm activity, Geophys. Res. Lett., 42, 2079-2087, https://doi.org/10.1002/2015GL063225, 2015.

Turner, D. L., O’Brien, T.P., Fennell, J.F., Claudepierre, S. G., Blake, J. B., Jaynes, A. N., Baker, D. N., Kanekal, S., Gkioulidou, M., Henderson, M. G., and Reeves, G. D.: Investigating the source of near-relativistics and relativistics electrons in Earth’s inner radiation belt, J. Geophys. Res. Space Physics, 122, 695-710, https://doi.org/ 10.1002/2016JA023600, 2017.

Vorobjev, V. G., Yagodkina,O. I., Sibeck, D. G., Liou,K., and Meng,C.-I. : Polar UVI observations of dayside auroral transient events, J. Geophys. Res., 106, 28,897–28,911, doi:10.1029/2000JA000396, 2001.

Zhao, H., and Li, X.: Modeling energetic electron penetration into the slot region and inner radiation belt, J. Geophys. Res. Space Physics, 118, 6936-6945, https://doi.org/10.1002/2013JA019240, 2013.

Zhao, H., Li, X., Baker, D.N., Claudepierre, S.G., Fennell, J. F., Blake, J. B., Larsen, B. A., Skoug, R. M., Funsten, H. O., Friedel, R. H. W., Reeves, G. D., Spence, H. E., Mitchell, D. G., and Lanzerotti, L. J.: Ring current electron dynamics during geomagnetic storms based on the

Van Allen Probes measurements, J. Geophys. Res. Space Physics, 121, 3333-3346, https://doi.org/10.1002/2016JA022358, 2016.

Zhao, H., Baker, D.N., Califf, S., Li, X., Jaynes, A. N., Leonard, T., Kanekal, S. G., Blake, J. B., Fennell, J. F., Claudepierre, S. G., Turner, D. L., Reeves, G. D., and Spence, H. E.: Van Allen Probes measurements of energetic particle deep penetration into the low L region (L<4) during the storm on 8 April 2016, J. Geophys. Res., 122, 12140-12152, https://doi.org/10.1002/2017JA024558, 2017a.

Zhao, H., Baker, D. N., Jaynes, A. N., Li, X., Elkington, S. R., Kanekal, S. G., Spence, H. E., Boyd, A. J., Huang, C.-L., and Forsyth, C.: On the relation between radiation belt electrons and solar wind parameters/geomagnetic indices: Dependence on the first adiabatic invariant and L*, J. Geophys. Res. Space Physics, 122, 1624-1642, https://doi.org/10.1002/2016JA023658, 2017b.

Wang, B., Nishimura, Y., Heitala, H., Lyons, L., Angelopoulos, V., Plaschke,F., Ebihara,Y., and Weatherwax, A.: Impacts of magnetosheath high-speed jets on the magnetosphere and ionosphere measured by optical imaging and satellite observations, J. Geophys. Res. Space Physics, 123, 4879-4894, https://doi.org/10.1002/2017JA024954, 2018.

Table 1 *FEE Enhancements observed by POES satellites*

FEE ID #	POES s/c ID	Observed time hh:mm UT	Longitude deg	LT* h
F1	P8	12:50	-164.2	1.8
F2	P5	13:15	-128.8	5.1
F3	P6	13:53	-138.3	5.1
F4	P8	14:32	169.7	1.6
F5	P5	14:54	-152.7	5.1
F6	P6	15:34	-162.5	5.0
F7	P2	15:44	-98.7	9.3
F8	P5	16:33	-170.1	5.0
F9	P7	16:37	-107.3	9.7
F10	P6	17:12	180.0	4.9
F11	P2	17:24	-123.0	9.4
F12	P7	18:16	-131.0	9.8
F13	P2	19:06	-140.0	9.6
F14	P8	20:30	-105.0	13.8
F15	P6	23:09	-94.5	17.2

* Local time

Table 2 *Timing of Magnetic Field Enhancements and Plasma Pulses from THEMIS and GOES12*

ID #	s/c ID	UT of magnetic peak hhmm:ss	UT of TH-D magnetosheath jet hhmm:ss	UT of TH-C foreshock pressure pulse hhmm:ss
1	TH-D	1333:40		~1328
	TH-E	1333:40		
	TH-B	1333:40		
	G12	1335:40		
2	TH-D	1420:50		~1417
	TH-E	1420:50		
	TH-B	1420:50		
	G12	1420:50		
3	TH-D	1550:30		~1549
	TH-E	1547:30		~1533, 1538
	G12	1544:00		
4	TH-D	1614:05	~1615 - 1616	~1611
	TH-E	1614:05		
	G12	1614:00		
5	TH-D	1638:20	~1640	~1634, 1636
	TH-E	1638:40		
	G12	1639:00		
6	TH-D	1647:45	~1648	absent
	TH-E	1647:45		
	G12	1648:00		
7	TH-D	-	~1651:30	absent
	TH-E	-		
8	TH-D	magnetosheath	~1700:30	~1700
	TH-E	-		
9	TH-D	magnetosheath	~1712 - 1713	~1707
	TH-E	1712:30		
10	TH-D	1722:30	~1725	~1718
	TH-E	1722:30		
	G12	1722:30		

Table 3

Location of Magnetic Stations in Geographic and Geomagnetic coordinates

Code	Name	GLat[a]	GLon[a]	MLat[b]	MLon[b]
AAE	Addis Ababa	9.0	38.8	5.3	109.9
ABG	Alibag	18.6	72.9	9.5	144.4
ASC	Ascension Island	-8.0	-14.4	-1.4	54.7
ASP	Alice Springs	-23.8	133.9	-34.1	-153.6
BNG	Bangui	4.3	18.6	4.6	89.3
CMO	College	64.9	-147.9	64.8	-102.6
CNB	Canberra	-35.3	149.4	-43.8	-134.5
CTA	Charters Towers	-20.1	146.3	-29.1	-140.7
EYR	Eyrewell	-43.4	172.4	-47.8	-107.0
GUA	Guam	13.6	144.9	4.2	-146.3
GZH	Zhaoqing	23.0	112.5	11.7	-177.1
HON	Honolulu	21.3	-158.0	21.2	-92.7
KAK	Kakioka	36.2	140.2	26.2	-153.3
KDU	Kakadu	-12.7	132.5	-23.2	-156.3
KNY	Kanoya	31.4	130.9	20.7	-161.2
KOU	Kourou	5.2	-52.7	16.1	17.7
MBO	Mbour	14.4	-17.0	21.1	55.8
MCQ	McQuarie Island	-54.5	159.0	-60.9	-116.2
MMB	Memambetsu	43.9	144.2	34.2	-150.9
PET	Paratunka	53.0	158.3	45.6	-138.5
PHU	Phuthuy	21.0	106.0	9.7	176.0
PPT	Pamatai	-17.6	-149.6	-15.2	-76.5
SHU	Shumagin	55.4	199.5	54.1	-103.1
SIT	Sitka	57.1	-135.3	60.1	-83.7
TSU	Tsumeb	-19.2	17.6	-18.3	83.5
VSS	Vassouras	-22.4	-43.7	-12.1	24.6

[a] Geographic latitude and longitude

[b] Magnetic latitude and longitude

FIGURE CAPTIONS

Figure 1. Geographic distribution of >30 keV electron fluxes measured by five NOAA/POES satellites on August 1, 2008 for the time interval (a) 0-12 UT, before the electron flux enhancements and (b) 12-24 UT, during the enhancements. The electrons are detected in vertical direction. In the forbidden zone those electrons are quasi-trapped. The electron fluxes enhanced largely during nonstorm condition after 12 UT. The forbidden zone is bounded by L=1.2 (white lines) and located outside of the South Atlantic Anomaly (SAA) at equatorial-to-low latitudes. Drift L-shells are calculated from IGRF-2005 model. The solid black curve indicates the dip equator.

Figure 2. FEE enhancements on 1 August 2008: (a) fluxes of >30 keV electrons in units $(cm^2\ s\ sr)^{-1}$, (b) L-shell of enhancements, (c) longitude and (d) local time of peak fluxes (black circles). Measurements within the SAA area are indicated by the open circles. Colorful curves denote NOAA/POES satellites: P2 (black), P5 (pink), P6 (red), P7 (blue), and P8 (green). Horizontal dashed line at panel (b) depicts the lower edge of the inner radiation belt. FEE enhancements peak at the equator (minimal L-shells) that indicates a fast radial transport from the inner radiation belt.

Figure 3. Solar wind parameters from OMNI data and geomagnetic indices on August 1, 2008. From top to bottom: (a) solar wind density (black) and dynamic pressure (blue), (b) solar wind speed, (c) interplanetary magnetic field (IMF) components Bx (blue), By (green), Bz (red) and magnitude B (black) in Geocentric Solar Magnetospheric (GMS) coordinates, (d) polar cap magnetic activity index PCN for northern (blue) and PCS for southern (red) hemispheres, (e) auroral electrojet index AE (black), AL (red), AU (green), and (f) storm time ring current variation index SYM-H. The shaded box denotes the time interval from 13 to 23 UT, when the nonstorm FEE enhancements were observed.

Figure 4. Spacecraft positions in GSM coordinates from 1200 to 1800 UT on August 1, 2018. The TH-C probe (blue) was in front of the subsolar bow shock. The TH-E (orange), TH-D (green), TH-B (brown), and GOES 12 (black) were located inside the dayside magnetosphere. The magnetopause position (black curve) was calculated using OMNI data for the upstream conditions at ~1600 UT following the model by Lin et al.'s (2010).

Figure 5. Observations of plasma and magnetic field on August 1, 2008. (a) Ion spectrogram (ion flux is in units of $eV/cm^2\ s\ sr\ eV$) and IMF vector components in GSM coordinates measured by TH-C, (b) IMF vector components from OMNI data set. Comparison of OMNI and TH-C data: (c) IMF cone angles plotted for OMNI (black) and TH-C (pink), red curve shows TH-C smoothed cone angle. (d) Solar wind dynamic pressure for OMNI (black circle), ACE

(blue curve) and for TH-C (red curve). Grey curve shows TH-C total pressure (sum of dynamic, magnetic and thermal pressures). The ACE data are shifted by 60 min.

Figure 6. Satellite measurements of magnetic field and plasma in the dayside magnetosphere and geomagnetic activity. (a) The Bz-GSM components from THEMIS probes TH-B (brown), TH-E (orange), and TH-D (green). The left y-axis corresponds to the magnetic measurements from TH-B and TH-D, and the right y-axis to TH-E. (b) The detrended magnetic fields for THEMIS. (c) The GOES-12 (black) and GOES-10 (blue) measurements of magnetic field strength (left y-axis) and local time (right y-axis). (d) The SYM-H index; and (e) the ion spectrogram from TH-D (ion flux is in units of eV/cm^2 s sr eV). Dashed lines, numbered from 1 to 10, indicate magnetic and plasma disturbances observed by THEMIS.

Figure 7. Observations of plasma and magnetic field at 1530-1800 UT on August 1, 2008: (a,b) ion spectrograms measured by TH-C, TH-D (ion flux is in units of eV/cm^2 s sr eV), (c) horizontal magnetic field Hp detected by GOES 12 from 10 to 13 LT, (d) magnetic field strengths Btot from TH-D (green) and TH-E (red), (e) IMF cone angles for TH-C (black) and for the ACE upstream monitor (blue). (f) TH-C solar wind dynamic pressure. Dashed lines and numbers 4 - 10 mark plasma structures of magnetosheath ions observed inside the magnetosphere.

Figure 8. Observations of plasma and magnetic field during the intervals 1600 - 1630 UT, 1630 - 1700 UT and 1658 - 1728 UT on August 1, 2008. Panels show from top to bottom: (a) ion spectrogram from TH-D, (b) total pressure Ptot measured by the ACE upstream monitor (black) and TH-D (red), (c) plasma density D measured by ACE (black) and TH-D (blue), (d) TH-D measurements of bulk velocity V (black) and its components in GSM coordinates Vx (blue), Vy (green) and Vz (red), (e) transversal components of magnetic field Bx (blue) and By (green) from TH-D, (f) magnitude B and Bz component of magnetic field from TH-D, (g) magnitude B and Bz component of magnetic field from TH-E. The magnetosheath plasma penetration is denoted by dashed lines and numbers #4 - #10.

Figure 9. Relative variations in the horizontal component (H) of the geomagnetic field at low geomagnetic latitudes. Local time intervals are indicated near the station codes. The vertical lines depict magnetic peaks #1 - #3 at THEMIS (see Table 2). Bottom panel shows magnetic field B measured by GOES-12 (black) and detrended magnetic field from TH-D (green).

Figure 10. Relative variations in the horizontal component (H) of the geomagnetic field in the midnight (left) and predawn (right) sectors. The geomagnetic latitudes of the stations are indicated near station codes. The vertical lines depict magnetic peaks at THEMIS (see Table 2). Magnetic data from THEMIS and GOES satellites are shown at lower panels on the right.

Figure 11. Dynamics of the geomagnetic field and particles on 1 August 2008: (a) FEE enhancements, (b) plasma precipitation at high latitudes, and dayside magnetic field perturbations observed by (c) GOES-12 (black), TH-D (green) and TH-B (brown). The left y-axis corresponds to GOES-12, and the right y-axis to TH-D and TH-B. The numbers indicate the FEE injections at ~2 and ~5 LT (see Table 1), colors for POES satellite are the same as in Figure 2. Plasma precipitations are shown for the energy flux above the threshold of 0.5 (erg/sm^2 s) and are grouped in LT: 23 – 24 LT (light gray), 0 – 2 LT (gray), 5 – 6 LT (blue), 12.5 - 15 LT (red points), 15 – 16 LT (violet), and 19.5 – 21.5 LT (green).

(a) (b)

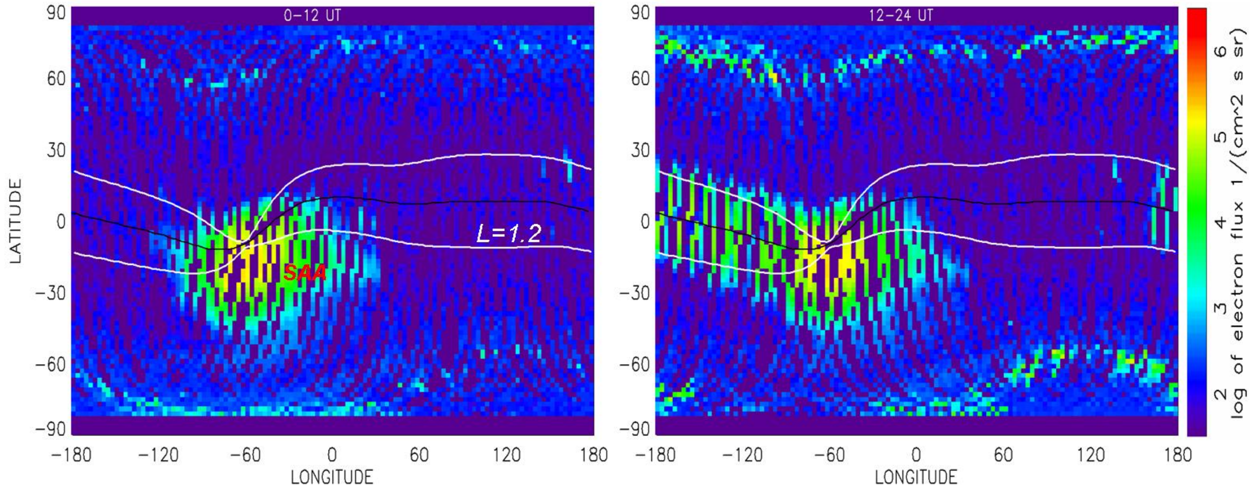

Figure 1. Geographic distribution of >30 keV electron fluxes measured by five NOAA/POES satellites on August 1, 2008 for the time interval (a) 0-12 UT, before the electron flux enhancements and (b) 12-24 UT, during the enhancements. The electrons are detected in vertical direction. In the forbidden zone those electrons are quasi-trapped. The electron fluxes enhanced largely during nonstorm condition after 12 UT. The forbidden zone is bounded by L=1.2 (white lines) and located outside of the South Atlantic Anomaly (SAA) at equatorial-to-low latitudes. Drift L-shells are calculated from IGRF-2005 model. The solid black curve indicates the dip equator. The

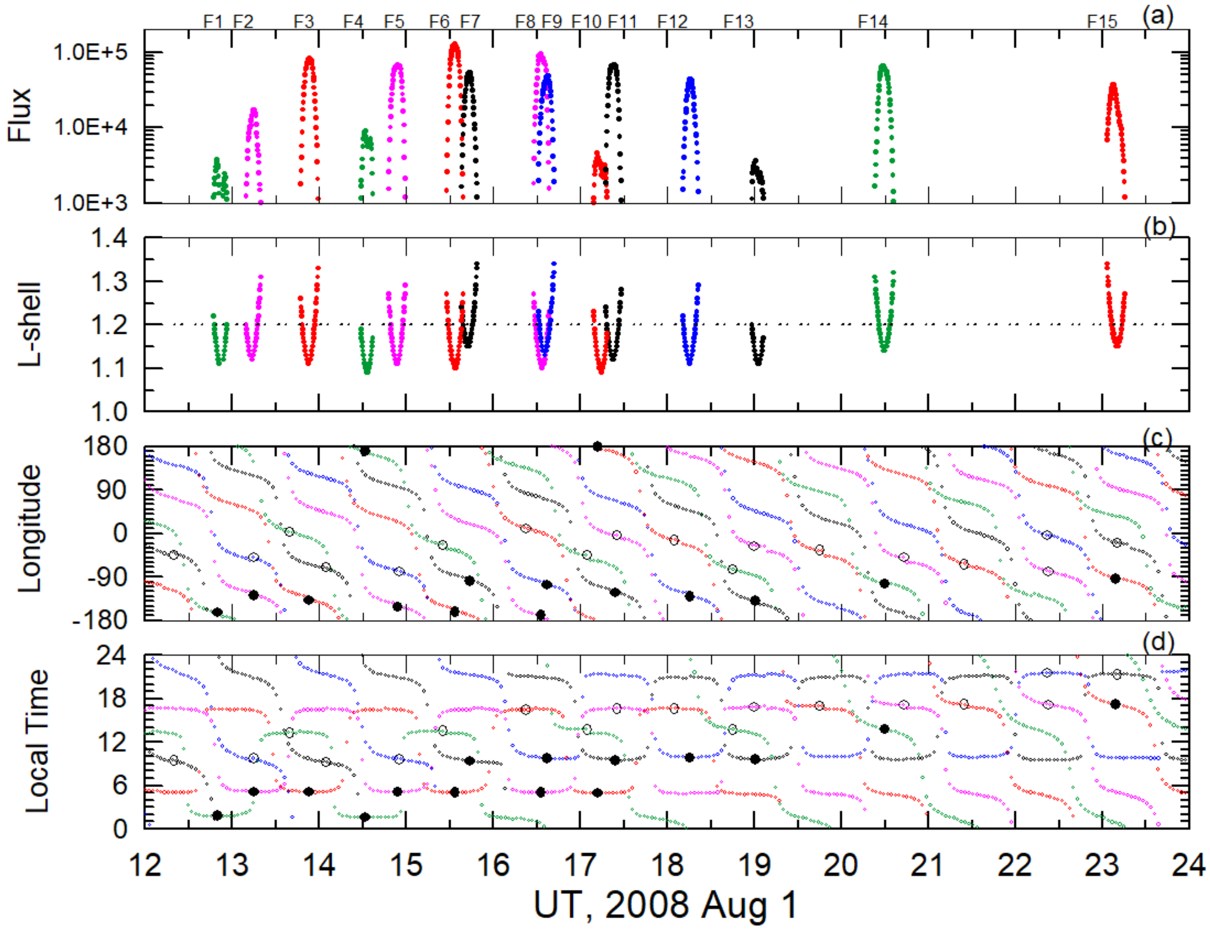

Figure 2. FEE enhancements on 1 August 2008: (a) fluxes of >30 keV electrons in units $(cm^2\ s\ sr)^{-1}$, (b) L-shell of enhancements, (c) longitude and (d) local time of peak fluxes (black circles). Measurements within the SAA area are indicated by the open circles. Colorful curves denote NOAA/POES satellites: P2 (black), P5 (pink), P6 (red), P7 (blue), and P8 (green). Horizontal dashed line at panel (b) depicts the lower edge of the inner radiation belt. FEE enhancements peak at the equator (minimal L-shells) that indicates a fast radial transport from the inner radiation belt.

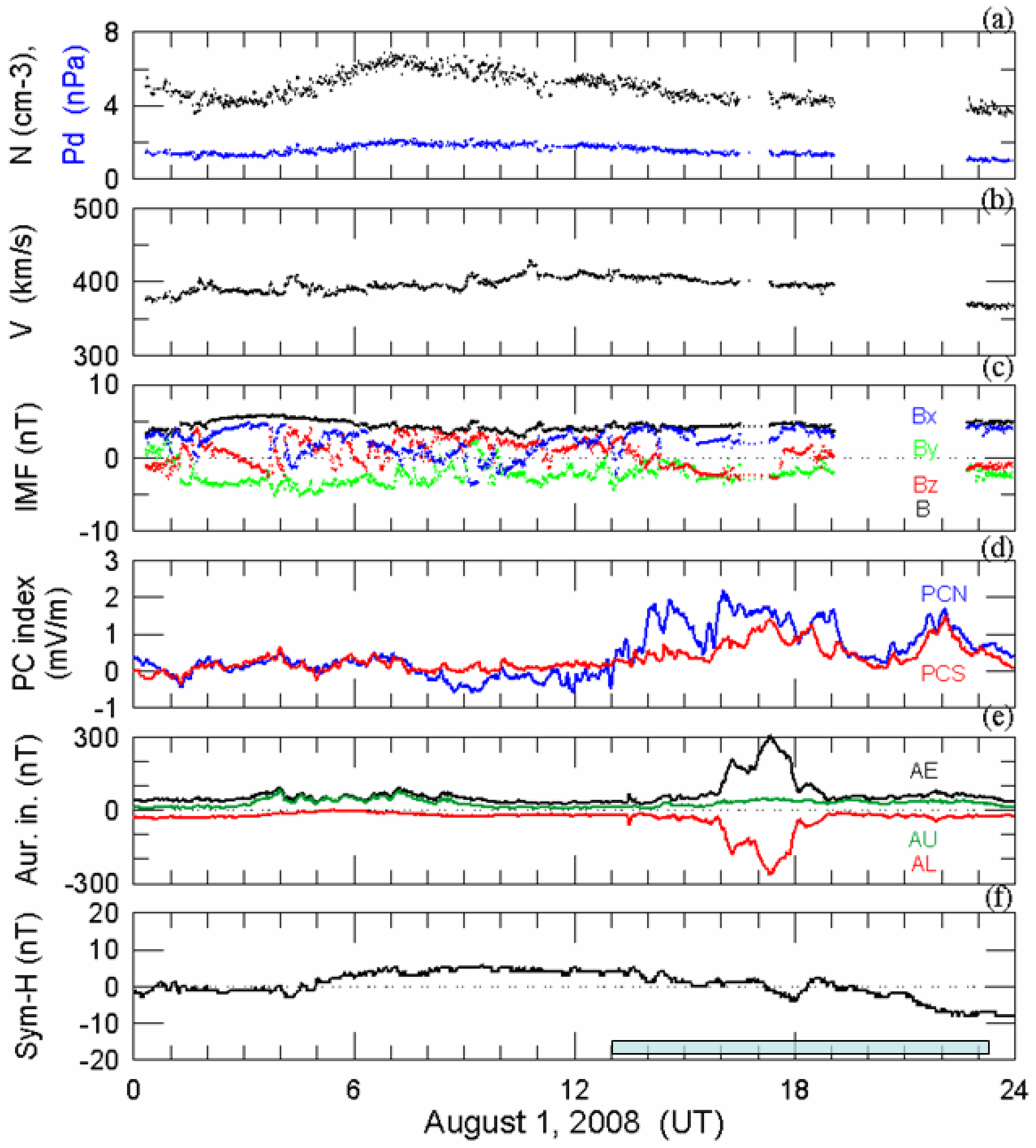

Figure 3. Solar wind parameters from OMNI data and geomagnetic indices on August 1, 2008. From top to bottom: (a) solar wind density (black) and dynamic pressure (blue), (b) solar wind speed, (c) interplanetary magnetic field (IMF) components Bx (blue), By (green), Bz (red) and magnitude B (black) in Geocentric Solar Magnetospheric (GMS) coordinates, (d) polar cap magnetic activity index PCN for northern (blue) and PCS for southern (red) hemispheres, (e) auroral electrojet index AE (black), AL (red), AU (green), and (f) storm time ring current variation index SYM-H. The shaded box denotes the time interval from 13 to 23 UT, when the nonstorm FEE enhancements were observed.

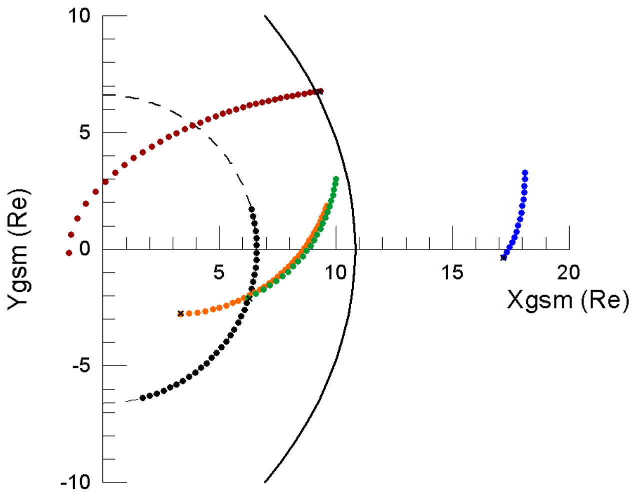

Figure 4. Spacecraft positions in GSM coordinates from 1200 to 1800 UT on August 1, 2018. The TH-C probe (blue) was in front of the subsolar bow shock. The TH-E (orange), TH-D (green), TH-B (brown), and GOES 12 (black) were located inside the dayside magnetosphere. The magnetopause position (black curve) was calculated using OMNI data for the upstream conditions at ~1600 UT following the model by Lin et al.'s (2010).

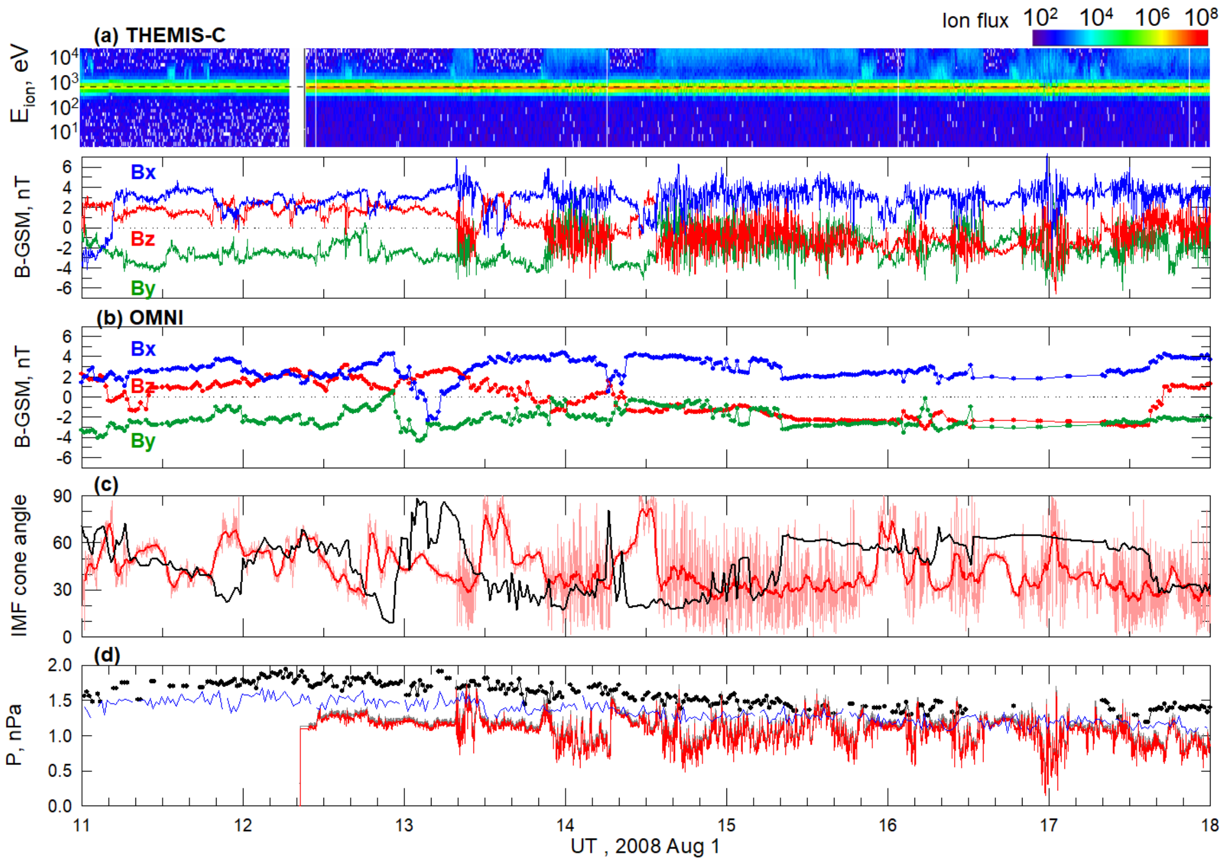

Figure 5. Observations of plasma and magnetic field on August 1, 2008. (a) Ion spectrogram (ion flux is in units of eV/cm^2 s sr eV) and IMF vector components in GSM coordinates measured by TH-C, (b) IMF vector components from OMNI data set. Comparison of OMNI and TH-C data: (c) IMF cone angles plotted for OMNI (black) and TH-C (pink), red curve shows TH-C smoothed cone angle. (d) Solar wind dynamic pressure for OMNI (black circle), ACE (blue curve) and for TH-C (red curve). Grey curve shows TH-C total pressure (sum of dynamic, magnetic and thermal pressures). The ACE data are shifted by 60 min.

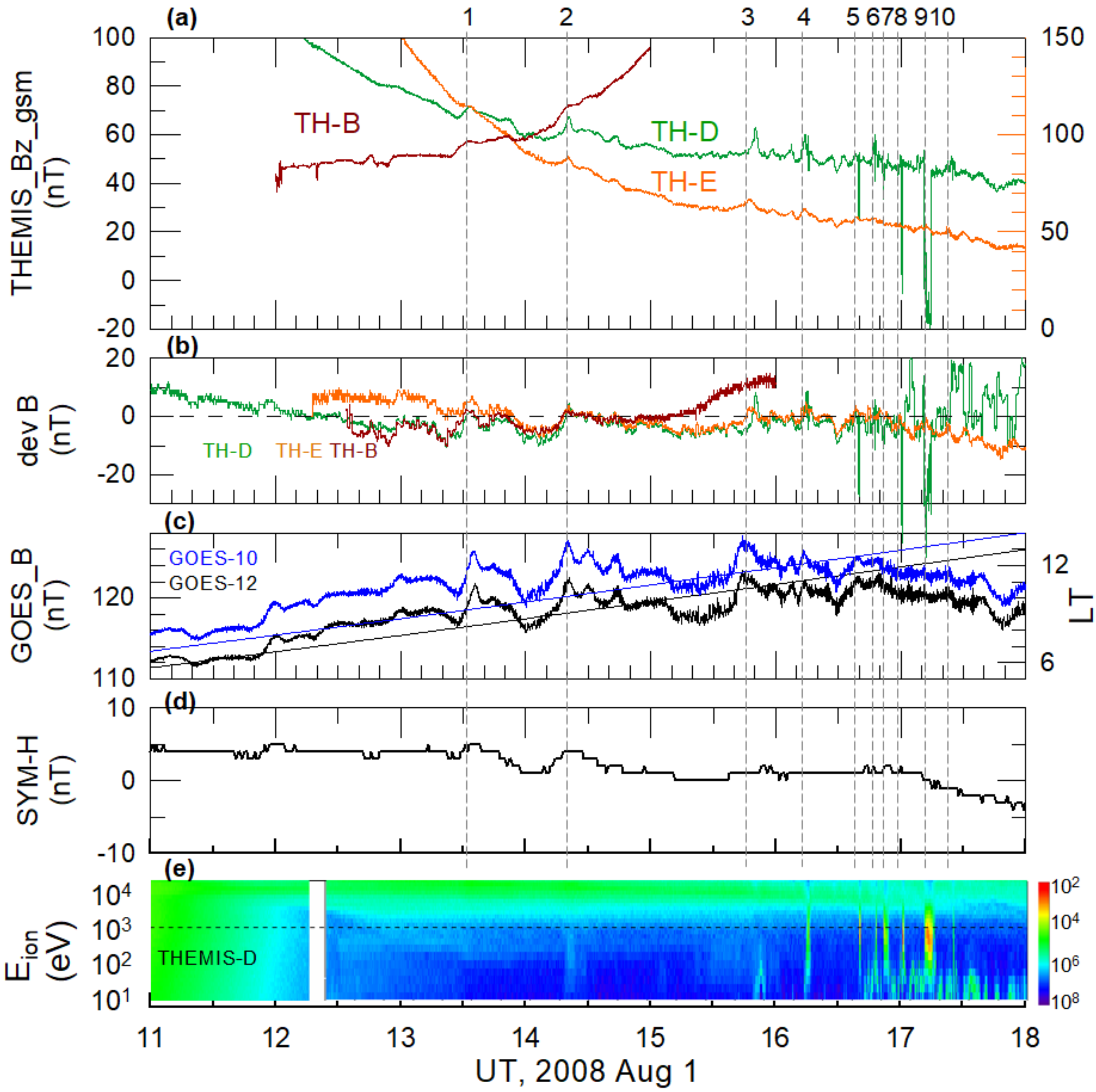

Figure 6. Satellite measurements of magnetic field and plasma in the dayside magnetosphere and geomagnetic activity. (a) The Bz-GSM components from THEMIS probes TH-B (brown), TH-E (orange), and TH-D (green). The left y-axis corresponds to the magnetic measurements from TH-B and TH-D, and the right y-axis to TH-E. (b) The detrended magnetic fields for THEMIS. (c) The GOES-12 (black) and GOES-10 (blue) measurements of magnetic field strength (left y-axis) and local time (right y-axis). (d) The SYM-H index; and (e) the ion spectrogram from TH-D (ion flux is in units of eV/cm^2 s sr eV). Dashed lines, numbered from 1 to 10, indicate magnetic and plasma disturbances observed by THEMIS.

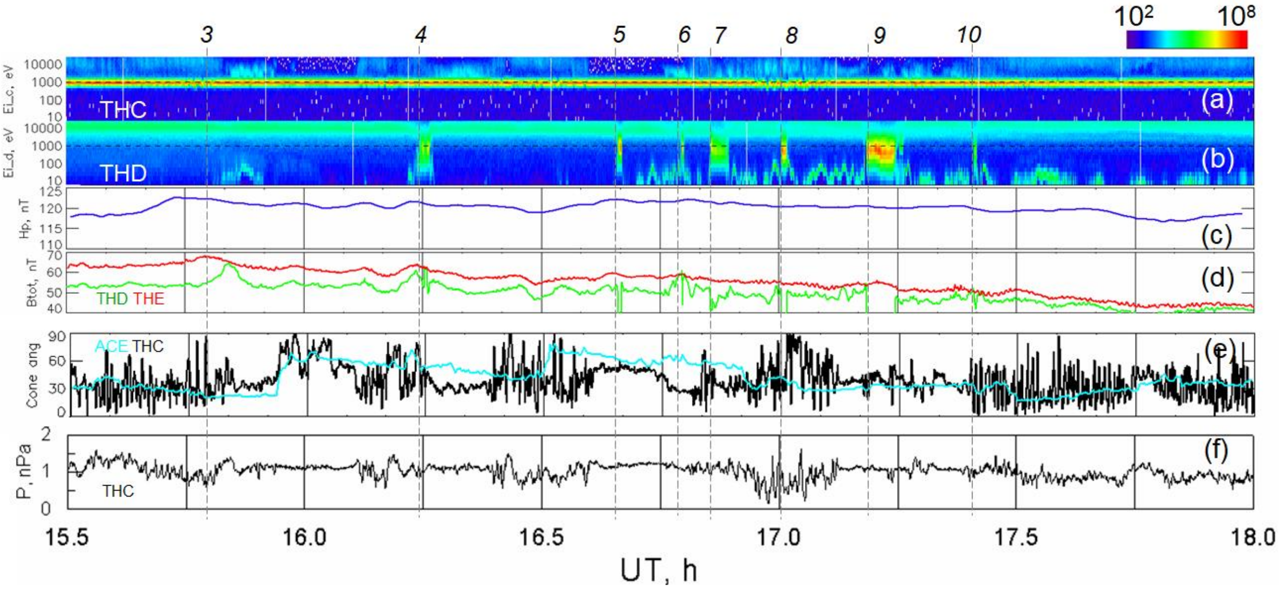

Figure 7. Observations of plasma and magnetic field at 1530-1800 UT on August 1, 2008: (a,b) ion spectrograms measured by TH-C, TH-D (ion flux is in units of eV/cm^2 s sr eV), (c) horizontal magnetic field Hp detected by GOES 12 from 10 to 13 LT, (d) magnetic field strengths Btot from TH-D (green) and TH-E (red), (e) IMF cone angles for TH-C (black) and for the ACE upstream monitor (blue). (f) TH-C solar wind dynamic pressure. Dashed lines and numbers 4 - 10 mark plasma structures of magnetosheath ions observed inside the magnetosphere.

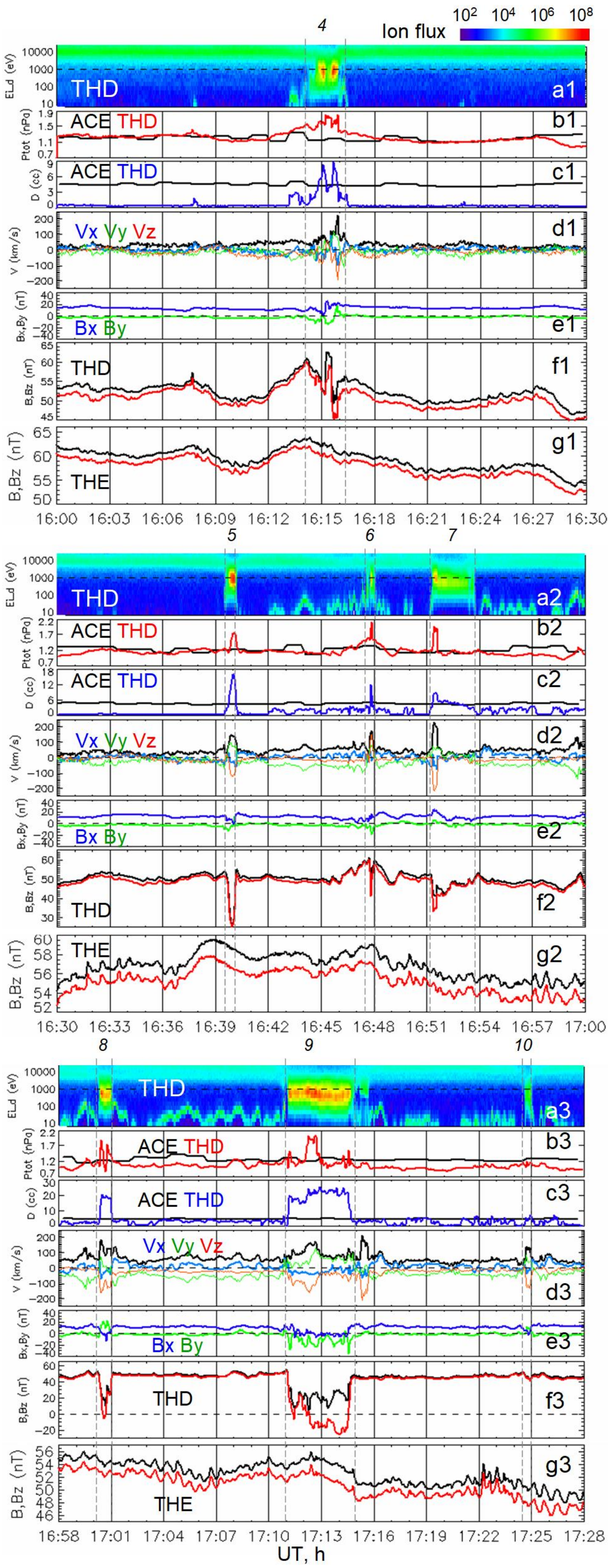

Figure 8. Observations of plasma and magnetic field during the intervals 1600 - 1630 UT, 1630 - 1700 UT and 1658 - 1728 UT on August 1, 2008. Panels show from top to bottom: (a) ion

spectrogram from TH-D, (b) total pressure measured by the ACE upstream monitor (black) and TH-D (red), (c) plasma density measured by ACE (black) and TH-D (blue), (d) TH-D measurements of bulk velocity V (black) and its components in GSM coordinates Vx (blue), Vy (green) and Vz (red), (e) transversal components of magnetic field Bx (blue) and By (green) from TH-D, (f) magnitude B and Bz component of magnetic field from TH-D, (g) magnitude B and Bz component of magnetic field from TH-E. The magnetosheath plasma penetration is denoted by dashed lines and numbers #4 - #10.

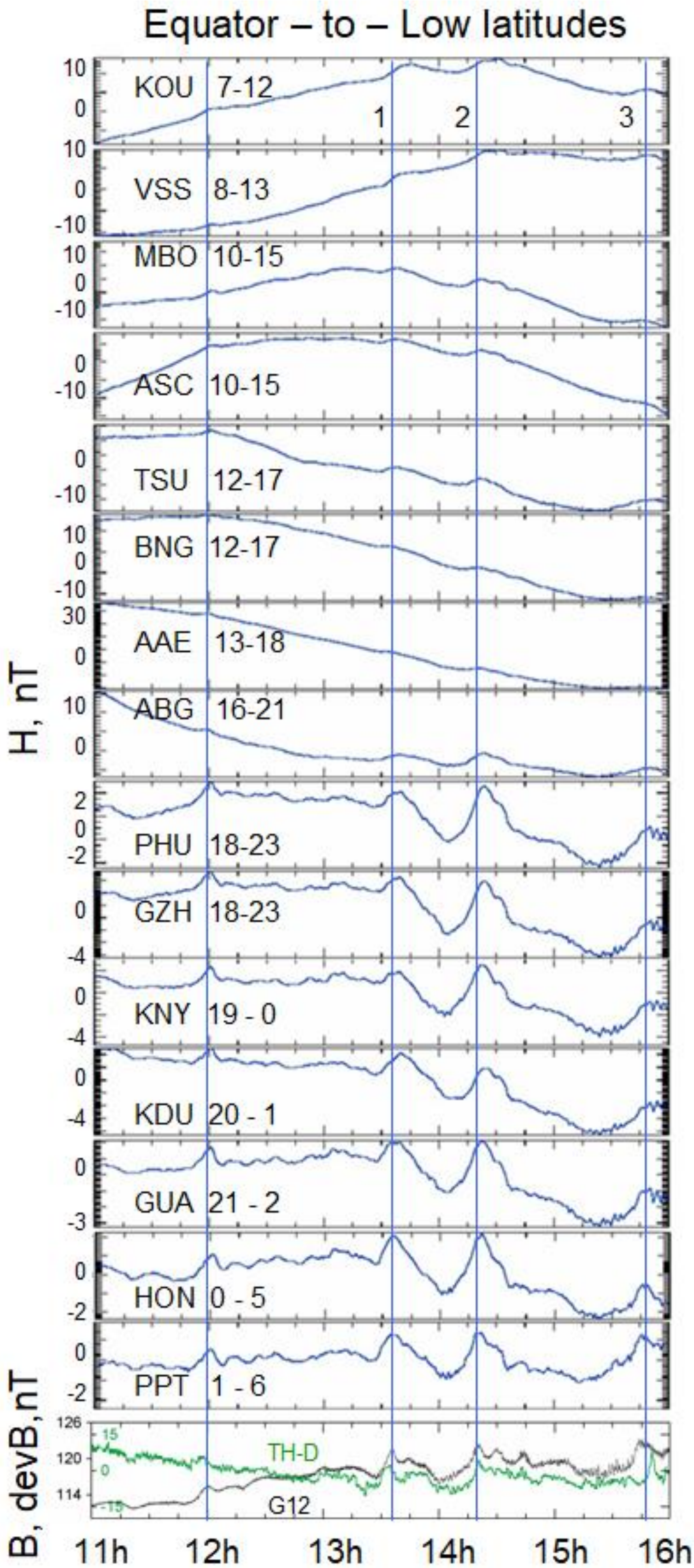

Figure 9. Relative variations in the horizontal component (H) of the geomagnetic field at low geomagnetic latitudes. Local time intervals are indicated near the station codes. The vertical lines depict magnetic peaks #1 - #3 at THEMIS (see Table 2). Bottom panel shows magnetic field B measured by GOES-12 (black) and detrended magnetic field from TH-D (green).

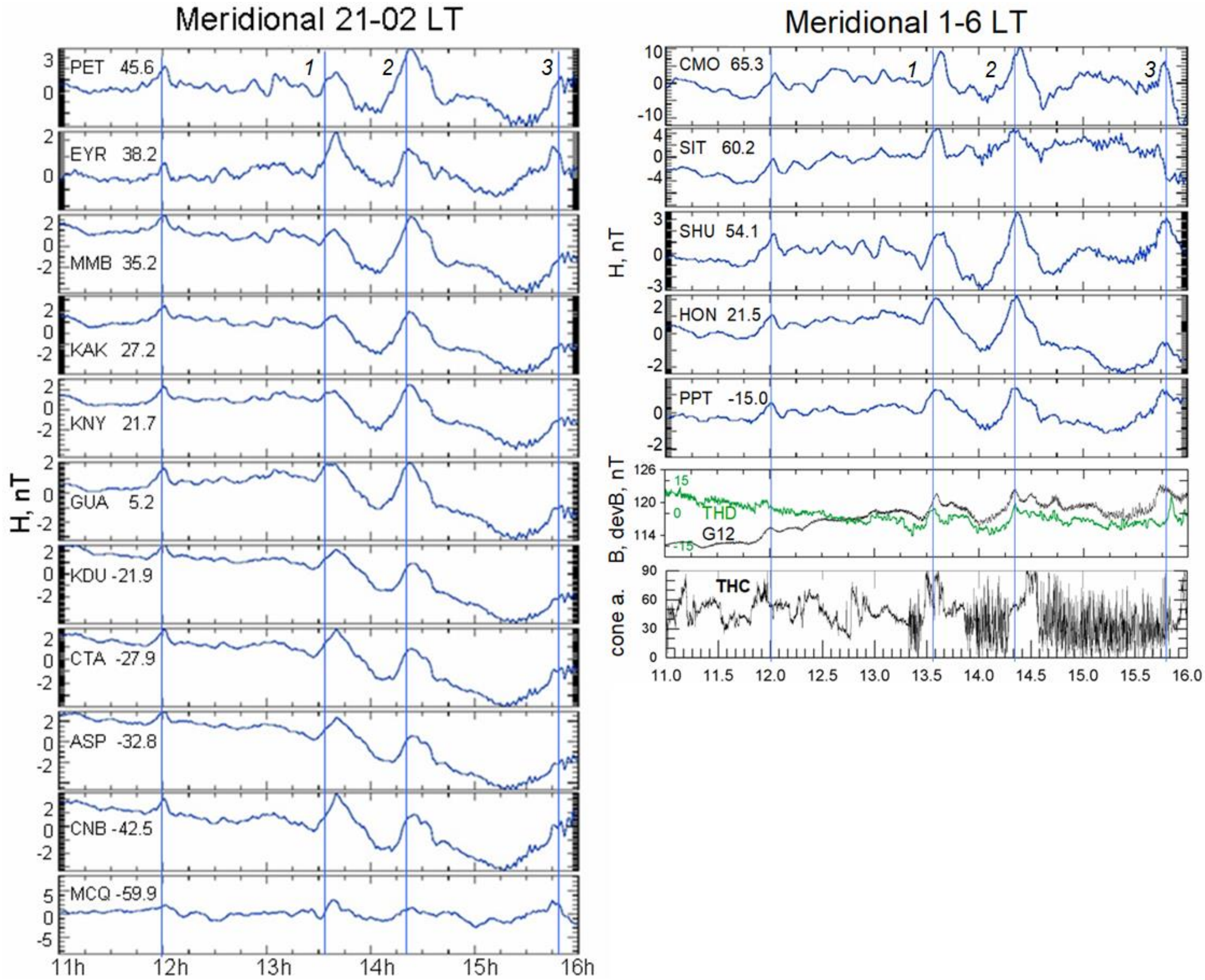

Figure 10. Relative variations in the horizontal component (H) of the geomagnetic field in the midnight (left) and predawn (right) sectors. The geomagnetic latitudes of the stations are indicated near station codes. The vertical lines depict magnetic peaks at THEMIS (see Table 2). Magnetic data from THEMIS and GOES satellites are shown at lower panels on the right.

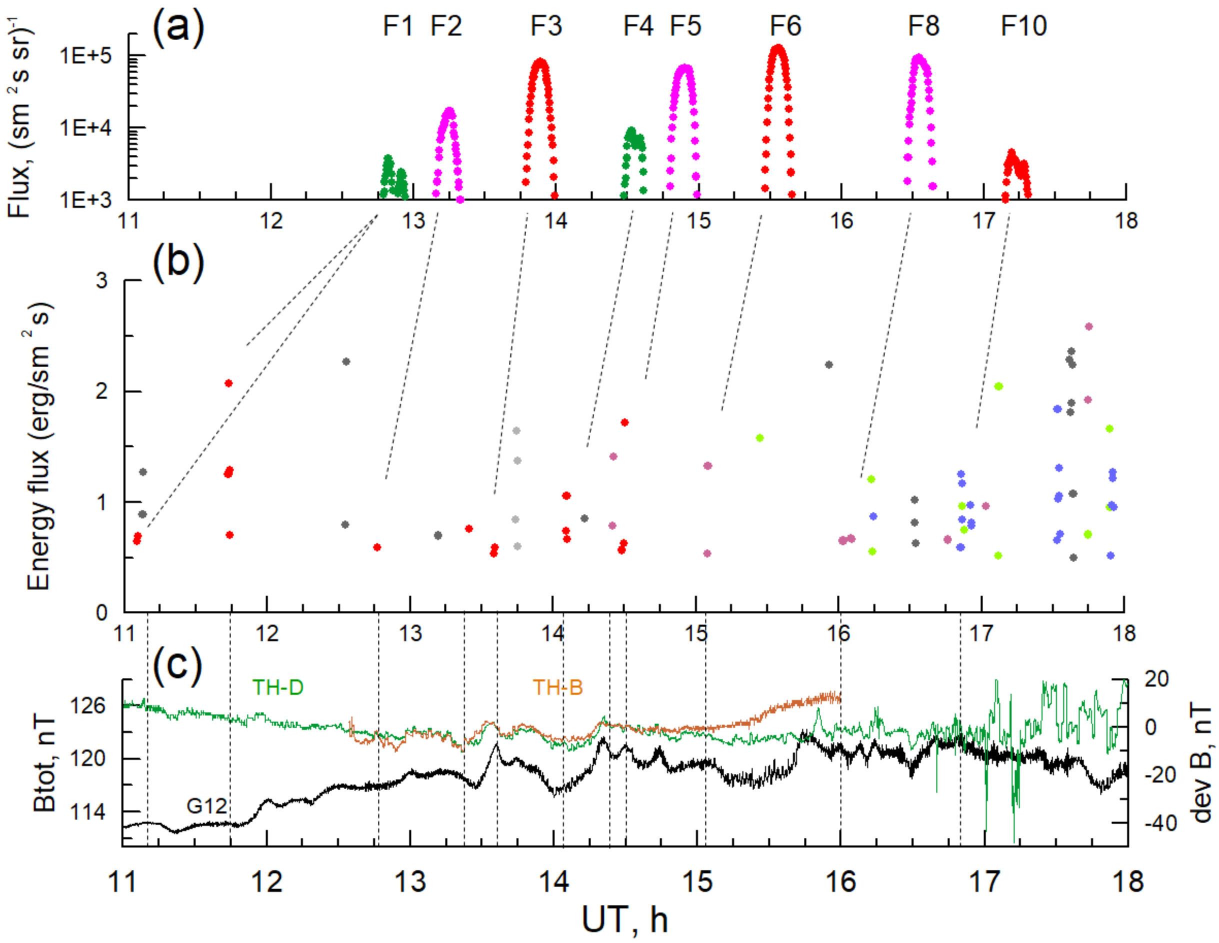

Figure 11. Dynamics of the geomagnetic field and particles on 1 August 2008: (a) FEE enhancements, (b) plasma precipitation at high latitudes, and dayside magnetic field perturbations observed by (c) GOES-12 (black), TH-D (green) and TH-B (brown). The left y-axis corresponds to GOES-12, and the right y-axis to TH-D and TH-B. The numbers indicate the FEE injections at ~2 and ~5 LT (see Table 1), colors for POES satellite are the same as in Figure 2. Plasma precipitations are shown for the energy flux above the threshold of 0.5 (erg/sm^2 s) and are grouped in LT: 23 – 24 LT (light gray), 0 – 2 LT (gray), 5 – 6 LT (blue), 12.5 - 15 LT (red points), 15 – 16 LT (violet), and 19.5 – 21.5 LT (green).